

# An efficient and robust method to estimate halo concentration based on the method of moments

Kai Wang <sup>1</sup>\*, H.J. Mo,<sup>2</sup> Yangyao Chen <sup>3,4</sup> and Joop Schaye <sup>5</sup>

<sup>1</sup>Kavli Institute for Astronomy and Astrophysics, Peking University, Beijing 100871, China

<sup>2</sup>Department of Astronomy, University of Massachusetts Amherst, MA 01003, USA

<sup>3</sup>School of Astronomy and Space Science, University of Science and Technology of China, Hefei, Anhui 230026, China

<sup>4</sup>Key Laboratory for Research in Galaxies and Cosmology, Department of Astronomy, University of Science and Technology of China, Hefei, Anhui 230026, China

<sup>5</sup>Leiden Observatory, Leiden University, PO Box 9513, 2300 RA Leiden, the Netherlands

Last updated 2020 May 22; in original form 2018 September 5

## ABSTRACT

We propose an efficient and robust method to estimate the halo concentration based on the first moment of the density distribution, which is  $R_1 \equiv \int_0^{r_{\text{vir}}} 4\pi r^3 \rho(r) dr / M_{\text{vir}} / r_{\text{vir}}$ . We find that  $R_1$  has a monotonic relation with the concentration parameter of the NFW profile, and that a cubic polynomial function can fit the relation with an error  $\lesssim 3\%$ . Tests on ideal NFW halos show that the conventional NFW profile fitting method and the  $V_{\text{max}}/V_{\text{vir}}$  method produce biased halo concentration estimation by  $\approx 10\%$  and  $\approx 30\%$ , respectively, for halos with 100 particles. In contrast, the systematic error for our  $R_1$  method is smaller than 0.5% even for halos containing only 100 particles. Convergence tests on realistic halos in  $N$ -body simulations show that the NFW profile fitting method underestimates the concentration parameter for halos with  $\lesssim 300$  particles by  $\geq 20\%$ , while the error for the  $R_1$  method is  $\lesssim 8\%$ . We also show other applications of  $R_1$ , including estimating  $V_{\text{max}}$  and the Einasto concentration  $c_e \equiv r_{\text{vir}}/r_{-2}$ . The calculation of  $R_1$  is efficient and robust, and we recommend including it as one of the halo properties in halo catalogs of cosmological simulations.

**Key words:** methods: statistical - galaxies: halos - dark matter - large-scale structure of Universe

## 1 INTRODUCTION

Dark matter halos, as the building blocks of the cosmic structures in our Universe, are virialized objects formed by gravitational instability. The assembly of halos proceeds hierarchically, where small halos are formed early and merge with each other to form larger ones. The assembly history of dark matter halos correlates strongly to the halo structure, and many semi-analytical models have been proposed to explain this correlation and to predict halo structure from its assembly history (e.g. Navarro et al. 1997; Wechsler et al. 2002; Zhao et al. 2003a; Lu et al. 2006; Zhao et al. 2009; Correa et al. 2015; Diemer & Joyce 2019). In addition, galaxies are born in the centers of dark matter halos and evolve following the halo assembly process (see Mo et al. 2010, for a review), so that dark matter halos and galaxies are tightly related to each other. This motivates many attempts to model the galaxy-halo connection to understand galaxy formation and evolution (see Baugh 2006; Mo et al. 2010; Wechsler & Tinker 2018, for reviews). Clearly, it is of paramount importance to accurately characterize the structure of dark matter halos.

Numerical  $N$ -body simulations with collisionless cold dark

matter particles provide an essential tool to study the structure of dark matter halos. To begin with, dark matter halos are identified with a halo-finding algorithm, such as the Friends-of-Friends (FoF) algorithm (e.g. Huchra & Geller 1982; Davis et al. 1985). Based on the spherical collapse model, a dark matter halo is defined as the collection of particles within a radius within which the mean density reaches some chosen value. This radius is usually referred to as the virial radius,  $r_{\text{vir}}$ , and the total mass enclosed is the halo mass,  $M_{\text{vir}}$ . The radial density profiles of dark matter halos are found to be well described by the universal NFW function,

$$\rho(r) = \frac{\rho_0}{r/r_s(1+r/r_s)^2}, \quad (1)$$

specified by the two free parameters,  $r_s$  and  $\rho_0$ , or equivalently,  $M_{\text{vir}}$  and the halo concentration,  $c \equiv r_{\text{vir}}/r_s$  (Navarro et al. 1997).

However, the determination of the concentration parameter for simulated halos is not straightforward. Many methods have been used to estimate the concentration parameters of simulated halos from the spatial distribution of dark matter particles (e.g. Jing 2000; Klypin et al. 2001; Bullock et al. 2001; Wechsler et al. 2002; Zhao et al. 2003b,a; Duffy et al. 2008; Zhao et al. 2009; Klypin et al. 2011, 2016). One approach is to sample the radial density distribution of simulated halos in discrete bins and fit it with the NFW profile (e.g. Bhattacharya et al. 2013). This method has several shortcomings.

\* Contact e-mail: wkcosmology@gmail.com

Firstly, the estimated concentration is subject to the choice of discrete bins. The use of large bin sizes tends to smooth the gradient of the radial profile and to cause an underestimate of the halo concentration, while the use of too small bins can introduce too much noise. In general, it is difficult to find an optimal binning strategy, particularly when a halo is only sparsely sampled. Secondly, the fitting method relies on the prior choice of the halo profile, which is the NFW profile in this case. Therefore, any deviations from the NFW profile will make the output concentration biased (Einasto 1965; Navarro et al. 2004; Wang et al. 2020b). Finally, the fitting procedure is relatively time-consuming, making it difficult to do for the large number of halos found in large cosmological simulations.

To overcome some of the issues in the NFW profile fitting, other estimators of halo concentration have been proposed. One example is the method based on  $V_{\max}/V_{\text{vir}}$  (Klypin et al. 2001, 2011; Prada et al. 2012; Klypin et al. 2016), where  $V_{\max} = \text{MAX}(\sqrt{GM(<r)}/r)$  is the maximum of the circular velocity as a function of  $r$ , and  $V_{\text{vir}} = \sqrt{GM(<r_{\text{vir}})}/r_{\text{vir}}$  is the virial velocity. This quantity is closely related to the halo concentration for an NFW halo. However, this relation is ill-defined for halos with concentration below 2.16 (Klypin et al. 2001), since by definition  $V_{\max}$  cannot be smaller than  $V_{\text{vir}}$ . The halo concentration can also be inferred from  $r_{\text{f}}/r_{\text{vir}}$ , where  $r_{\text{f}}$  is the radius within which the mass is  $fM_{\text{vir}}$ , with  $0 < f < 1$  (e.g. Lang et al. 2015). In addition, there are also methods based on the integrated mass profile (Poveda-Ruiz et al. 2016) and the Voronoi Tessellation (Lang et al. 2015).

In this paper, we propose an efficient and robust method to estimate the concentration parameter of NFW halos based on the first moment of the density distribution. § 2 introduces the data we use in this study. § 3 introduces three different methods to estimate the halo concentration, and we test their performance in § 4. § 5 shows the mass-concentration relation obtained from the ELUCID simulation, to demonstrate the application of our method to large cosmological simulations. § 6 discusses other applications of  $R_1$ , including estimating  $V_{\max}$  of halos and the Einasto concentration parameter. Finally, § 7 summarizes our main results. Throughout this paper, we use “log” to denote 10-based logarithm.

## 2 DATA

The estimation of halo concentration is subject to the sampling effect, where low-mass halos are poorly sampled in  $N$ -body simulations, and the force softening effect, which can smooth the density profile in the inner region and cause an underestimation of the halo concentration (e.g. Power et al. 2003; Ludlow et al. 2019; Mansfield & Avestruz 2021). To separate the impact of these two effects, we use two different datasets to test the performances of different methods: ideal halos generated from NFW profiles with different halo parameters, and realistic halos selected from  $N$ -body simulations of different resolutions and force softening lengths. We also apply our method to a large  $N$ -body simulation to demonstrate its capability of recovering halo concentrations in large cosmological simulations.

### 2.1 Ideal NFW halos

We generate ideal NFW halos using the HALOFACTORY package based on Eddington’s inversion method (see appendix A for details). Here we use halos with four different concentrations,  $c = 1, 5, 10$ , and 20, a range sufficient to cover halos in cosmological  $N$ -body simulations. For each concentration, we generate individual halos

using different numbers of particles, ranging from  $\sim 100$  to  $\gtrsim 10^4$ , to test the robustness of a given concentration estimator. For a given particle number, we use 10,000 random realizations to evaluate the statistical uncertainties.

## 2.2 $N$ -body simulations

### 2.2.1 IllustrisTNG-Dark

The IllustrisTNG project consists of several dark-matter-only and hydrodynamical simulations (Pillepich et al. 2018; Nelson et al. 2019). Here we use the dark-matter-only simulations with different resolutions and gravitational softening lengths to test the impact on the concentration estimation. The information of these simulations is summarized in Table 1 (Nelson et al. 2019). It is noteworthy that TNG100-1-Dark and TNG100-3-Dark have identical initial conditions, but different mass resolutions and gravitational softening lengths. The IllustrisTNG project was based on a cosmology consistent with the results in Planck Collaboration et al. (2016), where  $\Omega_{\Lambda} = 0.6911$ ,  $\Omega_{\text{m}} = 0.3089$ ,  $\sigma_8 = 0.8159$ ,  $n_s = 0.9667$ , and  $h = 0.6774$ . Dark matter halos are identified using the Friends-of-Friends algorithm with a linking length that is 0.2 the mean inter-particle distance (Davis et al. 1985), and their masses are assigned as the total dark matter mass enclosed within the aperture where the mean overdensity is 200 times the critical density. This mass is denoted as  $M_{200\text{c}}$ , and the corresponding radius and concentration are denoted as  $r_{200\text{c}}$  and  $c_{200\text{c}}$ , respectively. The halo center is specified as the location of the particle with the minimal gravitational potential. Substructures are identified with the SUBFIND algorithm (Springel et al. 2001).

### 2.2.2 ELUCID

The ELUCID<sup>1</sup> simulation (Wang et al. 2013, 2014, 2016; Tweed et al. 2017) is a constrained simulation, run with a memory-optimized version of GADGET-2 (Springel et al. 2005) known as L-GADGET, to reconstruct the density field and formation history of our local Universe based on the Sloan Digital Sky Survey DR7 (York et al. 2000). It is thus one particular realization of the structure formation model in question. This simulation has  $3072^3$  dark matter particles, each with a mass of  $3.09 \times 10^8 h^{-1} M_{\odot}$ , in a box with a side length of  $500 h^{-1} \text{Mpc}$ . This simulation assumes a  $\Lambda\text{CDM}$  cosmology with  $\Omega_{\text{m}} = 0.258$ ,  $\Omega_{\Lambda} = 0.742$ ,  $\sigma_8 = 0.80$ ,  $n_s = 0.96$ , and  $h = 0.72$ . The information of the ELUCID simulation is summarized in Table 1 (Wang et al. 2016). ELUCID uses the same procedure as IllustrisTNG to identify and define dark matter halos (see § 2.2.1). The large volume and relatively high resolution of the ELUCID simulation allow us to investigate the mass-concentration relation over a large halo mass range.

## 3 METHOD

Here we introduce three methods to estimate halo concentration: two commonly used methods and our  $R_1$  method. In addition, three other methods are discussed in Appendix C together with their performance on ideal NFW halos.

<sup>1</sup> <https://www.elucid-project.com/>

**Table 1.** Summary of the  $N$ -body simulations used in this study.

Simulation	$L_{\text{box}} [h^{-1}\text{Mpc}]$	Particle number	Particle mass [ $h^{-1}M_{\odot}$ ]	Gravitational softening length [ $h^{-1}\text{kpc}$ ]
TNG50-1-Dark	35	2160 <sup>3</sup>	$3.7 \times 10^5$	0.2
TNG100-1-Dark	75	1820 <sup>3</sup>	$6.0 \times 10^6$	0.5
TNG100-3-Dark	75	455 <sup>3</sup>	$3.8 \times 10^8$	2.0
ELUCID	500	3072 <sup>3</sup>	$3.1 \times 10^8$	3.5

### 3.1 The $R_1$ method

The total mass of a dark matter halo is expressed as

$$M_{\text{vir}} = \int_0^{r_{\text{vir}}} 4\pi r^2 \rho(r) dr. \quad (2)$$

Here  $\rho(r)$  is the radial density profile and  $r_{\text{vir}}$  is the halo radius, which is usually defined as the radius within which the enclosed mean density just exceeds some chosen value. The dimensionless first moment of the density distribution,  $R_1$ , can be defined as

$$R_1 = \frac{1}{M_{\text{vir}} r_{\text{vir}}} \int_0^{r_{\text{vir}}} 4\pi r^3 \rho(r) dr, \quad (3)$$

which can be expressed analytically for an NFW profile as

$$R_1 = \frac{c - 2 \ln(1+c) + c/(1+c)}{c [\ln(1+c) - c/(1+c)]}. \quad (4)$$

Despite the complicated functional form, the relation between  $R_1$  and  $c$  is actually quite simple, as shown in Fig. 1. We fit both  $R_1(c)$  and  $c(R_1)$  with third-order polynomial functions:

$$\log R_1 = a_1 (\log c)^3 + a_2 (\log c)^2 + a_3 \log c + a_4, \quad (5)$$

$$\log c = b_1 (\log R_1)^3 + b_2 (\log R_1)^2 + b_3 \log R_1 + b_4,$$

$$a_1 = 0.0198, \quad a_2 = -0.086, \quad a_3 = -0.090, \quad a_4 = -0.230,$$

$$b_1 = -34.01, \quad b_2 = -43.91, \quad b_3 = -23.49, \quad b_4 = -3.48.$$

The bottom panels of Fig. 1 show the fractional difference between the relation in equation (4) and the fitting formula of equation (5). The fractional deviation is  $\lesssim 0.1\%$  for the  $R_1 - c$  relation and  $\lesssim 3\%$  for the  $c - R_1$  relation. We note that the relation between  $R_1$  and  $c$  depends neither on cosmology nor on the threshold density chosen to define dark matter halos.

### 3.2 The NFW profile fitting method

The halo concentration can also be estimated by fitting the density distribution with an NFW profile (e.g. [Bhattacharya et al. 2013](#)). One can start with the cumulative mass distribution for an NFW halo:

$$M(< r) = \frac{m(cr/r_{\text{vir}})}{m(c)} M_{\text{vir}}, \quad (6)$$

where

$$m(x) = \ln(1+x) - x/(1+x). \quad (7)$$

The optimal concentration can be found by minimizing the  $\chi^2$  defined as

$$\chi^2 = \sum_i \frac{(M_i^{\text{sim}} - M_i)^2}{(M_i^{\text{sim}})^2 / n_i}, \quad (8)$$

where  $M_i = M(< r_i) - M(< r_{i-1})$  is the mass within the  $i$ -th radial bin according to the NFW profile,  $M_i^{\text{sim}}$  is the total mass of particles in the same radial bin for the simulated halo, and  $n_i$  is the number of particles in that bin. Here we take 20 equally spaced radial bins

from  $0.01r_{\text{vir}}$  to  $r_{\text{vir}}$  on the logarithmic scale. Clearly, the result of the NFW profile fitting method is subject to the choice of binning. In Appendix B, we test the performance with three different binning strategies and adopt the best one here to compare with the other two methods.

### 3.3 The $V_{\text{max}}/V_{\text{vir}}$ method

For NFW halos, the concentration parameter is also related to the ratio between the maximum circular velocity and the virial velocity,

$$\frac{V_{\text{max}}}{V_{\text{vir}}} = \frac{\text{MAX}(V_{\text{circ}}(r))}{V_{\text{circ}}(r_{\text{vir}})}, \quad (9)$$

where  $V_{\text{circ}}(r) = \sqrt{GM(< r)/r}$ , and the relation is

$$\frac{V_{\text{max}}}{V_{\text{vir}}} = \left[ \frac{0.216c}{\ln(1+c) - c/(1+c)} \right]^{1/2} \quad (10)$$

(e.g. [Klypin et al. 2001](#)). Note that this relation is only applicable for  $c \gtrsim 2.16$  since  $V_{\text{max}} \geq V_{\text{vir}}$  by definition.

## 4 TESTING THE PERFORMANCE OF THE HALO CONCENTRATION ESTIMATORS

### 4.1 Tests on ideal NFW profile

We first test the performance of the three concentration estimation methods on ideal NFW halos generated from the HALOFACTORY package (see appendix A). The results are presented in Fig. 2. The four columns are for four different input halo concentrations, from  $c = 1$  to  $c = 20$ , and the three rows present the results for three different methods. In each panel, the red solid line shows the median fractional deviation of the concentration parameter estimated from 10,000 halo realizations as a function of particle number, and the magenta dashed lines and the cyan dotted lines show the 16<sup>th</sup> – 84<sup>th</sup> and 2.5<sup>th</sup> – 97.5<sup>th</sup> percentile ranges, respectively.

Firstly, when the particle number is sufficiently large ( $\gtrsim 10^4$ ), all three methods perform equally well and the fractional deviation of the halo concentration estimation for 95% of halo realizations is within  $\pm 5\%$ . Secondly, when the particle number decreases to a few hundred, the NFW profile fitting method tends to underestimate halo concentration by  $\approx 10\%$ . We note that this result is subject to the choice of binning (see Appendix B). The  $V_{\text{max}}/V_{\text{vir}}$  method tends to overestimate the halo concentration by  $\approx 30\%$ , which was already noted in previous studies (see [Poveda-Ruiz et al. 2016](#)). In contrast, the fractional deviation of the median value for our  $R_1$  method is less than 0.5%. Thirdly, the distribution of the estimated concentration broadens with decreasing particle numbers. When only 100 particles are used, the width of the 16<sup>th</sup> – 84<sup>th</sup> percentiles is about  $0.76c - 1.03c$  for the NFW fitting method,  $0.91c - 1.06c$  for the  $V_{\text{max}}/V_{\text{vir}}$  method, and  $0.63c - 0.91c$  for our  $R_1$  method. Therefore, the  $R_1$  method also yields the smallest variance among all three methods when halos are poorly sampled. We also note

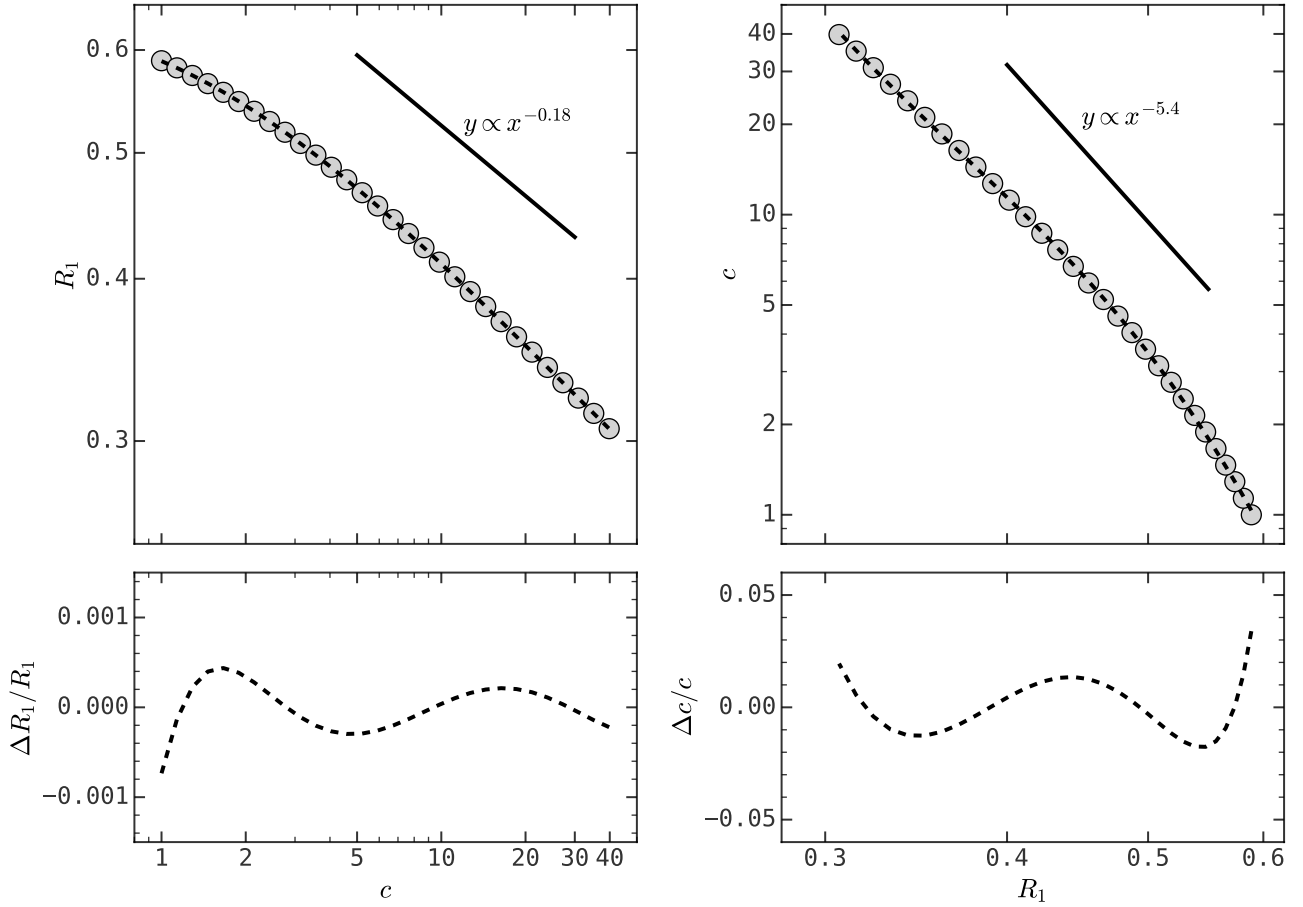


**Figure 1.** The relation between  $c$  and  $R_1$  for an NFW profile. Top panels: The circles are the analytical results obtained through equation (4), and the dashed lines are the fitted third-order polynomial functions in equation (5). Bottom panels: The fractional difference between the relation in equation (4) and the third-order polynomial fits.

that the  $V_{\max}/V_{\text{vir}}$  method is not applicable to halos with  $c \lesssim 2.16$ . In addition, Appendix C presents the performance of three other concentration estimation methods. Our test results show that their performances are poorer than the  $R_1$  method, even though some of them are more difficult to obtain from simulation data.

Finally, Appendix D shows the distributions of the logarithmic deviation of halo concentration estimated with our  $R_1$  method. These distributions can be described by Gaussian functions, and the scatter decreases with increasing particle number and decreasing input concentration. A fitting function is provided to describe the dependence of the scatter on the particle number and the input concentration (see equation (D2)).

## 4.2 Impact of resolution

We have already shown that our  $R_1$  method outperforms the other two methods in halo concentration estimation using ideal NFW halos. However, low-mass halos in realistic  $N$ -body simulations are not only poorly sampled, but also subject to the force softening used to avoid unphysical gravity when two particles are too close to each other (e.g. Power et al. 2003; Ludlow et al. 2019). In addition, halos in simulations are not spherically symmetric and are not perfectly relaxed (e.g. Jing 2000; Jing & Suto 2002). While it is not a priori

clear what the true concentration is for halos in simulations, we can investigate which method gives the best convergence with the numerical resolution.

Here we use three simulations from the IllustrisTNG suite, which are TNG50-1-Dark, TNG100-1-Dark, and TNG100-3-Dark, to test the impact of numerical resolution on the estimation of halo concentration. Note again that the latter two simulations use identical initial conditions and simulation code, but different mass resolutions and gravitational softening lengths (see table 1). Fig. 3 shows the mass-concentration relation obtained from these three simulations, and the top and bottom panels show results obtained from the NFW profile fitting method and our  $R_1$  method, respectively. Firstly, both methods produce nearly identical median mass-concentration relations and the 16<sup>th</sup> – 84<sup>th</sup> percentiles in TNG100-1-Dark, whose particle mass is about  $6.0 \times 10^6 h^{-1} M_\odot$ . Secondly, the NFW profile fitting method underestimates the concentration of  $10^{11} h^{-1} M_\odot$  halos ( $\lesssim 300$  particles) by  $\gtrsim 20\%$  in TNG100-3-Dark, whose particle mass is about  $3.8 \times 10^8 h^{-1} M_\odot$ . In contrast, the  $R_1$  method yields nearly identical mass-concentration relations across the entire mass range in these two simulations, and the fractional deviation for low-mass halos is  $\lesssim 8\%$  between the two simulations. Note that a  $10^{11} h^{-1} M_\odot$  halo in TNG100-3-Dark is represented by only  $\lesssim 300$  particles. Finally, the mass-concentration relations obtained from

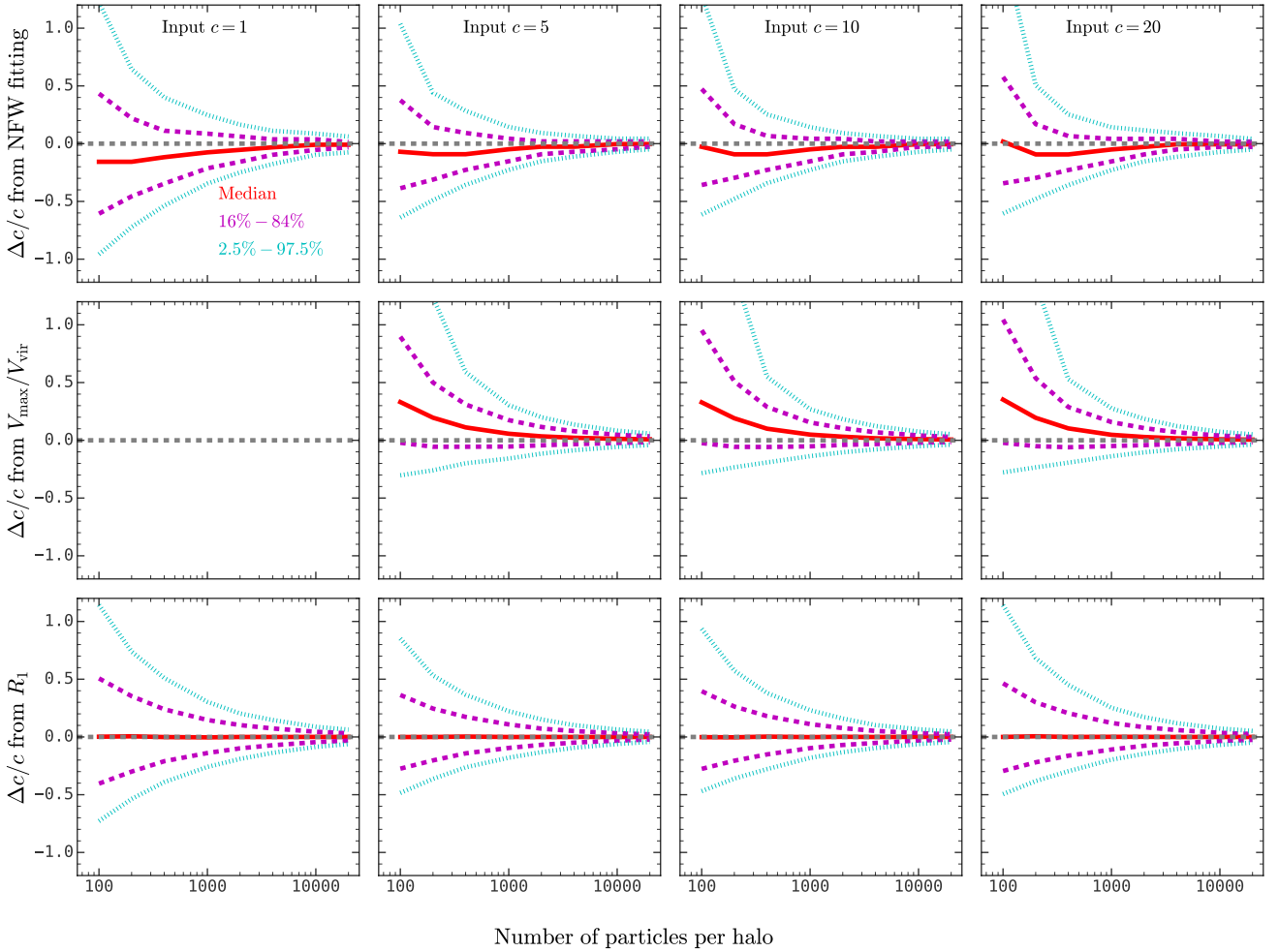


**Figure 2.** The fractional difference between the input and the estimated concentrations with the NFW fitting method (top panels), the  $V_{\max}/V_{\text{vir}}$  method (middle panels), and the  $R_1$  method (bottom panels) for ideal NFW halos generated with HALOFAC<sub>TORY</sub> as a function of the number of particles in the halo. The red solid, magenta dashed, and cyan dotted lines show the 50<sup>th</sup>, 16<sup>th</sup> – 84<sup>th</sup>, and 2.5<sup>th</sup> – 97.5<sup>th</sup> percentiles. This figure shows that the  $R_1$  method gives an unbiased and less uncertain estimation of the input halo concentration compared with the other two methods. The middle left panel is empty since the  $V_{\max}/V_{\text{vir}}$  method cannot be applied to halos with  $c < 2.16$ .

TNG50-1-Dark by the two methods are similar to each other, and to those obtained from TNG100-1-Dark. The discrepancy at the massive end owes to cosmic variance, since the two simulations have different box sizes and initial conditions. In Appendix G, we show that the concentration parameter  $c_{200c}$  can also be obtained from  $R_1$  with integrating only to  $r_{500c}$ , which is commonly used in observation.

Fig. 4 compares the halo concentration estimated with the NFW profile fitting method and our  $R_1$  method in the three TNG-Dark simulations, where open circles and error bars show the median and the 16<sup>th</sup> – 84<sup>th</sup> percentiles, respectively. Firstly, both methods yield similar concentrations for massive halos and low-concentration low-mass halos. Secondly, the NFW fitting method produces lower concentrations than our  $R_1$  method for high-concentration low-mass halos, and the discrepancy is larger in lower-resolution simulations. Combined with the results in Fig. 3, we infer that the NFW profile fitting method tends to underestimate the concentration of high-concentration low-mass halos in low-resolution simulations for two reasons. The first one is that the NFW profile

fitting method tends to underestimate halo concentration for poorly-sampled halos, as shown in Fig. 2, but this effect becomes marginal once more than a few thousand particles are sampled. The second reason is that, for a given simulation volume, the force softening length is larger in lower resolution runs, and so is a larger fraction of the virial radius in lower mass halos, and therefore has a large impact on the central mass profile. This will consequently cause the underestimation of halo concentration in the NFW profile fitting method. A common strategy to tackle this problem is to exclude particles below the convergence radius during the fitting, where the convergence radius is defined such that the two-body dynamical relaxation timescale of the particles within this radius is comparable to the age of the universe (Power et al. 2003; Duffy et al. 2008; Correa et al. 2015). However, the convergence radius is about  $0.1r_{200c}$  for halos with a few hundred particles (Ludlow et al. 2019), and excluding particles within this radius will cause systematic underestimations of the concentration parameter by  $\approx 20\% - 50\%$  for halos with  $c \approx 10 - 20$  for the NFW fitting method (see Appendix B). In con-

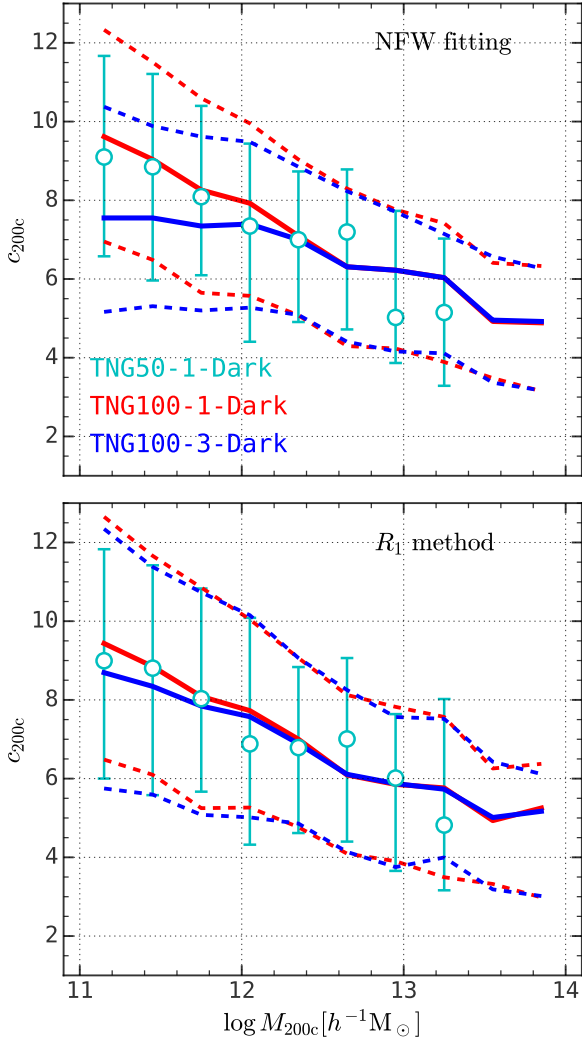


**Figure 3.** The mass-concentration relation for TNG50-1-Dark (cyan error bars), TNG100-1-Dark (red lines), and TNG100-3-Dark (blue lines), where the 16<sup>th</sup> – 50<sup>th</sup> – 84<sup>th</sup> percentiles are presented. The upper panel shows the result obtained with the NFW profile fitting method, and the lower panel shows the result obtained with our  $R_1$  method. The NFW profile fitting method underestimates halo concentration for low-resolution simulations, while this effect is marginal for our  $R_1$  method.

trast, the  $R_1$  method is less affected by the inclusion, since it gives more weight to the outer region of dark matter halos.

Finally, there is still a noticeable discrepancy between these two methods for high-concentration halos with  $M_{200c} \approx 10^{11} h^{-1} M_{\odot}$  in TNG100-1-Dark and TNG50-1-Dark, where a  $10^{11} h^{-1} M_{\odot}$  halo is well represented by  $\gtrsim 2.7 \times 10^5$  particles. In Appendix E, we find that these halos deviate from the NFW profile due to the stripping of mass in the outskirts, and the mass distribution recovered from both concentrations matches the data equally well, despite the  $\gtrsim 10\%$  systematics in the values of the estimated concentration. Nevertheless, these halos constitute only a small portion of all halos in the given mass bin, as one can see from the histogram in the top panels of Fig. 4.

## 5 THE MASS-CONCENTRATION RELATION IN THE ELUCID SIMULATION

It has been shown in § 4 that our  $R_1$  method outperforms the conventional method in the halo concentration estimation on both ideal NFW halos and realistic halos in  $N$ -body simulations, and it can give unbiased estimation of the concentration parameter for halos with more than 200 particles. For this reason, we apply the  $R_1$  method to the ELUCID simulation and infer the mass-concentration relation for halos with  $11 \lesssim \log(M_{200c}/[h^{-1}M_{\odot}]) \lesssim 15$ . Notably, a  $10^{11} h^{-1} M_{\odot}$  halo is only represented by about 300 particles in ELUCID.

Fig. 5 shows the median mass-concentration relation in ELUCID, as well as the 16<sup>th</sup> – 84<sup>th</sup> percentiles. Here relaxed and unrelaxed halos are separated according to the criterion in Neto et al. (2007), which is

$$\text{Relaxed halos : } \Delta < 0.07 r_{200c} \quad (11)$$

$$\text{Unrelaxed halos : } \Delta > 0.07 r_{200c}$$

$$\Delta = \|\mathbf{r}_{\text{min-pot}} - \mathbf{r}_{\text{com}}\|$$

where  $\mathbf{r}_{\text{min-pot}}$  is the position of the particle with the minimal gravitational potential, and  $\mathbf{r}_{\text{com}}$  is the center of mass of all dark matter particles within  $r_{200c}$ . Note that Neto et al. (2007) uses two additional conditions to select halos in equilibrium. They require that the mass fraction in substructures is lower than a threshold value and that the ratio between the kinetic energy and the potential energy is lower than a threshold. Here we use only the criterion in equation (11), for three reasons. Firstly, as shown in Neto et al. (2007), equation (11) alone can select most of the halos in equilibrium (see their Figure 2). Secondly, equation (11) is the simplest criterion to implement in  $N$ -body simulations, whereas the other two criteria require either identifying substructures or calculating the gravitational potential for each particle. Thirdly, the other two criteria suffer from some ambiguities. For instance, the substructure mass fraction is subject to the substructure finder used (e.g. van den Bosch & Jiang 2016) and to the resolution of the simulation (e.g. van den Bosch et al. 2018). Besides, the exact value of the virial ratio for selecting halos in equilibrium is still under debate, as many argued that the surface pressure and even the non-spherical shape of halos should be taken into account (e.g. Davis et al. 2011; Klypin et al. 2016). Here one can see that the concentration parameter decreases from  $\approx 8$  to  $\approx 4$  with increasing mass for relaxed halos, and from  $\approx 4$  to  $\approx 2$  for unrelaxed ones. It has already been noted in previous studies that unrelaxed halos exhibit lower concentration than relaxed ones (e.g. Jing 2000; Neto et al. 2007; Duffy et al. 2008; Child et al. 2018). A detailed analysis in Wang et al. (2020a) reveals that a sudden halo-halo merger event will reduce the concentration dramatically, and the concentration parameter will gradually increase during the subsequent secular evolution. For comparison, the solid lines show the mass-concentration relations given by seven different semi-analytical models with the same cosmology and halo definition<sup>2</sup>. Our results are broadly consistent with these models.

In addition to the median mass-concentration relation, the distribution of concentration at given halo masses also carries important information. Fig. 6 shows the distribution of the logarithmic halo concentration,  $\log c$ , for relaxed and unrelaxed halos in four narrow halo mass bins. For each halo population in a given mass

<sup>2</sup> All these models are implemented in the CoLOSSUS package (Diemer 2018), except Zhao+09 (<http://202.127.29.4/dhzhao/mandc.html>) and Correa+15 (<https://www.camilacorrea.com/code/commah/>).

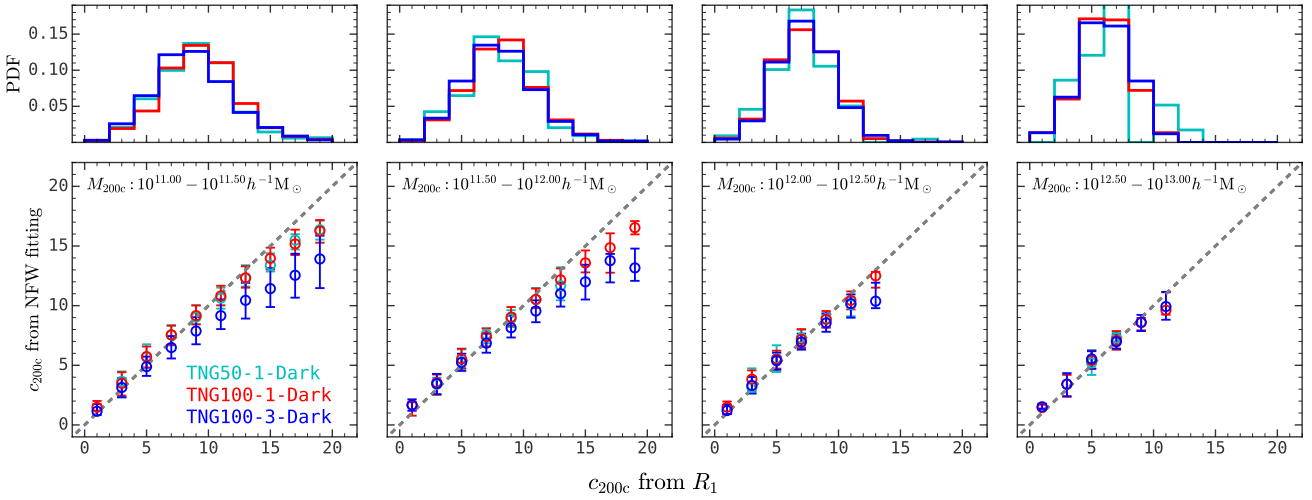


**Figure 4.** Top panels: The probability distribution function of halo concentration estimated with our  $R_1$  method in three TNG-Dark simulations. Bottom panels: Comparison of halo concentration estimated from the NFW profile fitting method and our  $R_1$  method in different halo mass bins. When combined with Fig. 3, this figure demonstrates that, compared with our  $R_1$  method, the NFW fitting method underestimates halo concentration for halos sampled with small numbers ( $\leq 300$ ) of particles, especially for high-concentration halos.

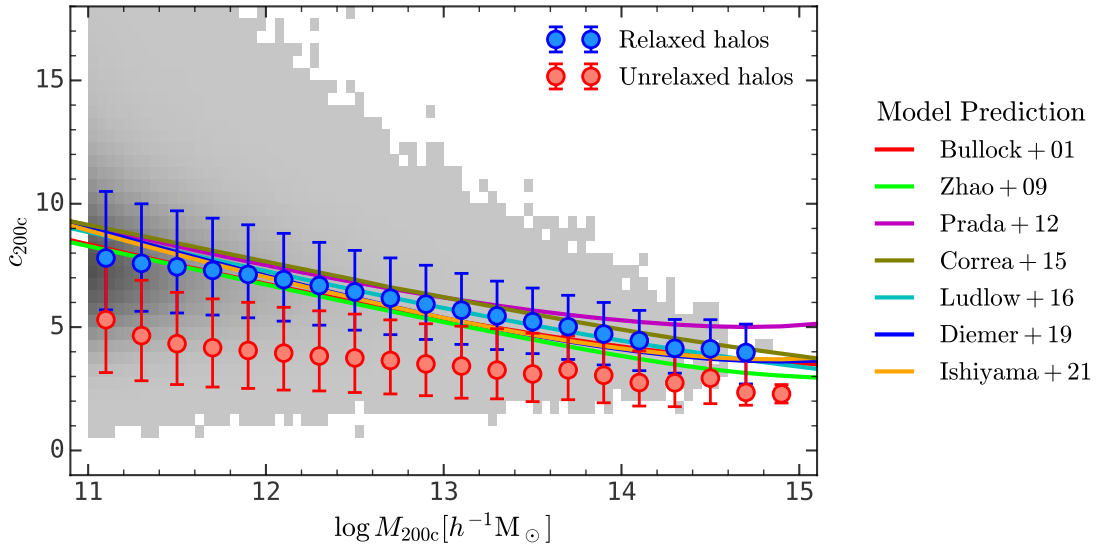
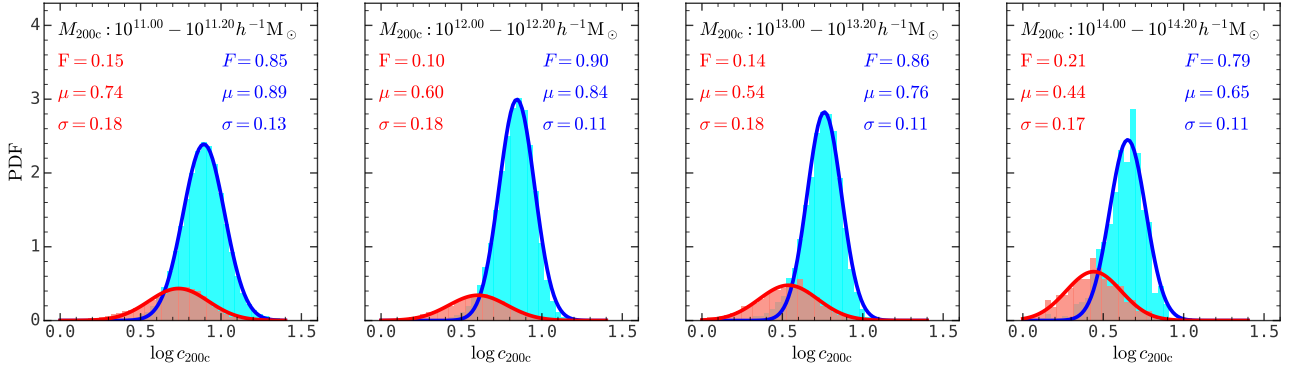


**Figure 5.** The mass-concentration relation in the ELUCID simulation for relaxed (blue error bars) and unrelaxed (red error bars) halos, and the 16<sup>th</sup> – 84<sup>th</sup> percentiles. The gray color scale encodes the number density of dark matter halos. The criterion for separating relaxed and unrelaxed halos is shown in equation (11). The solid lines are the predictions of different semi-analytical models: Bullock+01 (Bullock et al. 2001), Zhao+09 (Zhao et al. 2009), Prada+12 (Prada et al. 2012), Correa+15 (Correa et al. 2015), Ludlow+16 (Ludlow et al. 2016), Diemer+19 (Diemer & Joyce 2019), and Ishiyama+21 (Ishiyama et al. 2021).

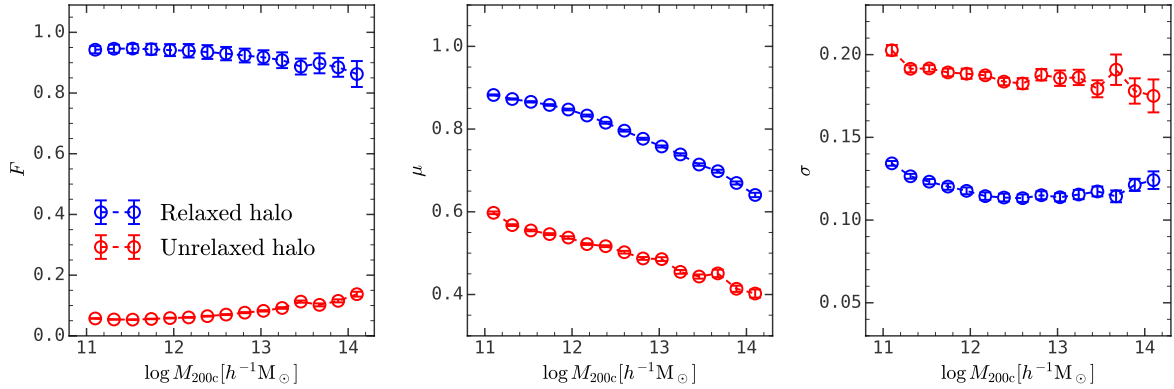
bin, we fit the distribution of  $\log c$  to a Gaussian function. Each distribution is thus described by three parameters:  $F$  as the fraction of the target halo population among all halos in the same mass bin,  $\mu$  as the mean of the Gaussian function, and  $\sigma$  as the standard deviation. The fitting functions are shown in blue and red solid lines in Fig. 6 for relaxed and unrelaxed halos, respectively. One can see that the Gaussian model describes the distribution quite well.

Fig. 7 shows the halo mass dependence of these fitting parameters. First of all, the unrelaxed halos only amounts to about 5% of

all halos with  $M_{200c} \approx 10^{11} h^{-1} M_{\odot}$ , and this fraction increases to about 15% for  $10^{14} h^{-1} M_{\odot}$  halos. The positive correlation between the unrelaxed halo fraction and halo mass is expected, since the halo merger rate is positively correlated to halo mass (e.g. Fakhouri & Ma 2008). Secondly, the mean logarithmic concentration declines with increasing halo mass for both relaxed and unrelaxed halos, with a constant gap of about 0.28 dex. Finally, the scatter in the distribution of  $\log c$  for relaxed and unrelaxed halos are about 0.12 and 0.19 dex, respectively, with a weak dependence on halo mass.



**Figure 6.** The distribution of the logarithmic halo concentration in four mass bins for relaxed (blue) and unrelaxed (red) halos, where the criterion to separate these two populations is shown in equation (11). The distribution of both halo populations are fitted with a Gaussian function as shown in solid lines. The best-fitting parameters are shown on the panel.



**Figure 7.** The halo mass dependence of the fitting parameters for relaxed (blue) and unrelaxed (red) halos, where the left panel shows the halo fraction  $F$ , the middle panel the mean  $\log c$ , and the right panel the standard deviation of  $\log c$ .

## 6 OTHER APPLICATIONS OF $R_1$

### 6.1 Estimating $V_{\max}$ from $R_1$

The maximum circular velocity,  $V_{\max}$ , is not only a proxy of halo concentration, but also a commonly-adopted quantity to connect galaxies with their dark matter halos (Reddick et al. 2013; Matthee et al. 2017; Zehavi et al. 2019). It is thus important to be able to obtain  $V_{\max}$  efficiently and robustly for a large sample of simulated halos in order to investigate the galaxy-halo connection using large cosmological simulations. To this end, we derive  $V_{\max}$  from  $R_1$  according to equations (4) and 10. Fig. 8 compares the  $V_{\max}/V_{\text{vir}}$  calculated from equation (9) and derived from  $R_1$ , where one can see they match quite well. We note that there is a small discrepancy for low-mass halos with high  $V_{\max}/V_{\text{vir}}$ , which has the same origin as the discrepancy for low-mass halos with high concentrations shown in Fig. 4 (see also Appendix E). Nevertheless, these halos only account for a small portion of all halos at the given halo mass bin, as shown in the top panels of Fig. 8. The relative rank is well preserved, as indicated by high Spearman’s rank correlation coefficients ( $\geq 0.92$ ).

It should be noted that  $R_1$  is defined only for main halos<sup>3</sup>. For a satellite subhalo contained in a host halo, one can trace its main-branch progenitor to the snapshot prior to the infall into its host halo and calculate its  $R_1$  to derive  $V_{\max}$ . This is similar to the calculation of  $V_{\text{peak}}$ , which is the peak value of  $V_{\max}$  on the main branch and serves as a better proxy in subhalo abundance matching than  $V_{\max}$  (Reddick et al. 2013). However, it is unclear whether or not environmental effects prior to the infall of halos can break the relation between  $V_{\max}$  and  $R_1$ . To test the validity of the  $R_1$  method for subhalos, we compare results between pre-infall halos at a given redshift, defined as halos that will become subhalos in the subsequent snapshot, and the results are presented in Appendix H. There one can see that the  $V_{\max} - R_1$  relation does not depend on whether or not halos are soon falling into other halos to become a satellite, indicating that the  $R_1$  method can also be used to estimate  $V_{\text{peak}}$  for subhalos.

<sup>3</sup> In principle the  $R_1$  method can also be used for stripped satellite subhalos provided the core survives. The integral in equation (3) should then be stopped before the virial radius at some  $R_{\Delta}$  with  $\Delta > 200$  (see Appendix G).

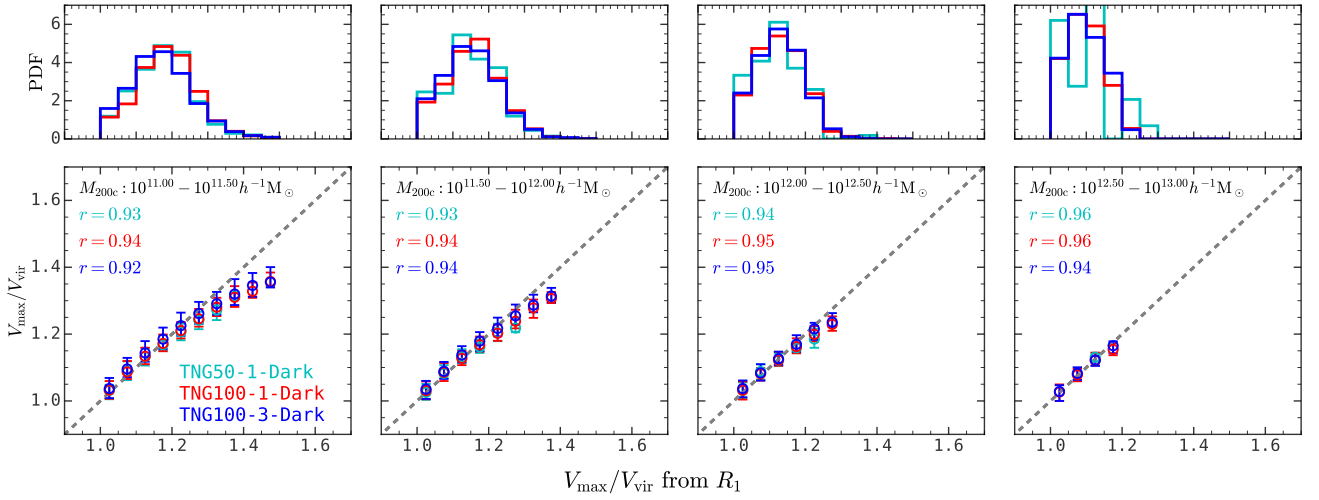


**Figure 8.** Top panels: The probability distribution of  $V_{\max}/V_{\text{vir}}$  estimated from  $R_1$  in three TNG-Dark simulations. Bottom panels: Comparison of  $V_{\max}/V_{\text{vir}}$  calculated from equation (9) and from our  $R_1$  method in three TNG-Dark simulations. Spearman's rank correlation coefficients are labeled on the bottom panels.

## 6.2 Estimating the Einasto concentration from $R_1$

It has been suggested that the radial density distribution of dark matter halos in  $N$ -body simulations is better fitted with a three-parameter Einasto profile (Navarro et al. 2004; Gao et al. 2008; Wang et al. 2020b), which has the form

$$\rho(r) = \rho_{-2} \exp \left\{ -\frac{2}{\alpha} \left[ \left( \frac{r}{r_{-2}} \right)^\alpha - 1 \right] \right\}, \quad (12)$$

where  $\rho_{-2}$ ,  $\alpha$ , and  $r_{-2}$  are free parameters. Gao et al. (2008) found that there is a universal relationship between  $\alpha$  and the peak height  $\nu$  given by

$$\alpha = 0.155 + 0.0095\nu^2, \quad \nu = \delta_{\text{crit}}(z)/\sigma(M_{\text{vir}}, z) \quad (13)$$

where the peak height  $\nu$  is defined as the ratio between the critical overdensity  $\delta_{\text{crit}}(z)$  for collapse at redshift  $z$  and the linear rms fluctuation at  $z$  within spheres containing mass  $M_{\text{vir}}$ . We note that the value of  $\nu$  is determined by redshift and halo mass for a given cosmology. The typical value of  $\alpha$  is between 0.15 and 0.3. The concentration parameter for the Einasto profile is defined as

$$c_e \equiv r_{\text{vir}}/r_{-2}. \quad (14)$$

Therefore, at a given redshift of  $z$ , the halo mass  $M_{\text{vir}}$  and the Einasto concentration  $c_e$  together determine the halo density profile, with the parameter  $\alpha$  determined by equation (13).

Fig. 9 shows the relation between  $R_1$  and the Einasto concentration  $c_e$  for  $0.15 \leq \alpha \leq 0.3$  in circles. And the solid lines are the fitting function,

$$c_e = d_1 x^3 + d_2 x^2 + d_3 x + d_4 \quad (15)$$

$$x = \frac{R_1}{\alpha^{0.95}} + e_1 \alpha^3 + e_2 \alpha^2 + e_3 \alpha + e_4$$

$$d_1 = -5.45, \quad d_2 = 14.72, \quad d_3 = -18.70, \quad d_4 = 9.07$$

$$e_1 = 191.32, \quad e_2 = -173.00, \quad e_3 = 57.78, \quad e_4 = -8.06$$

The bottom panel shows the fractional residual, from which one can see that this fitting function is accurate to  $\lesssim 5\%$  for  $c_e \gtrsim 3$  and  $\lesssim 10\%$  for  $c_e \lesssim 3$ .

## 7 SUMMARY

Estimating the concentration parameter and related quantities of simulated dark matter halos in large numerical  $N$ -body simulations is a critical step to study halo structure and understand its relation to the halo assembly history and to the properties of galaxies that form in them. A reliable and efficient method is needed to estimate these quantities for large cosmological simulations that include halos with a wide range of particle numbers. To this end, we propose an efficient and robust method to estimate the halo concentration and related quantities using the first moment of the density distribution. Our main results are summarized as follows:

(i) We find that the first moment of the density distribution, defined as  $R_1 = \int_0^{r_{\text{vir}}} 4\pi r^3 \rho(r) dr^3 / M_{\text{vir}} / r_{\text{vir}}$ , has a simple, monotonic relation with the halo concentration for NFW halos. A cubic polynomial function can describe this relation to  $\lesssim 3\%$  accuracy (see Fig. 1).

(ii) Testing on ideal NFW halos, we find that the NFW profile fitting method and the  $V_{\max}/V_{\text{vir}}$  method introduce  $\approx 10\%$  and  $\approx 30\%$  systematics for halos with 100 particles. In contrast, the bias introduced by the  $R_1$  method is smaller than 0.5%. The  $R_1$  method yields the smallest variance among all the three methods.

(iii) Testing on realistic halos in  $N$ -body simulations of different resolutions, we find that the NFW fitting method underestimates the concentration parameter of halos with  $\lesssim 300$  particles by  $\gtrsim 20\%$ , due to the poor sampling and the large gravitational softening length. In contrast, such effects only introduce  $\lesssim 8\%$  systematics in the  $R_1$  method (see Figs. 3 and 4).

(iv) We apply the  $R_1$  method to the ELUCID  $N$ -body simulation and obtain the mass-concentration relation across four orders of magnitude of halo mass, separately for relaxed and unrelaxed halos. We find that the distributions of the logarithmic concentration,  $\log c$ , for both populations can be described by a Gaussian function. We find that the fraction of unrelaxed halos ranges from  $\approx 5\%$  to  $\approx 15\%$  from  $10^{11} h^{-1} M_\odot$  to  $10^{14} h^{-1} M_\odot$ . The mean logarithmic concentration declines monotonically with halo mass for both relaxed and unrelaxed halos, and there is a constant difference

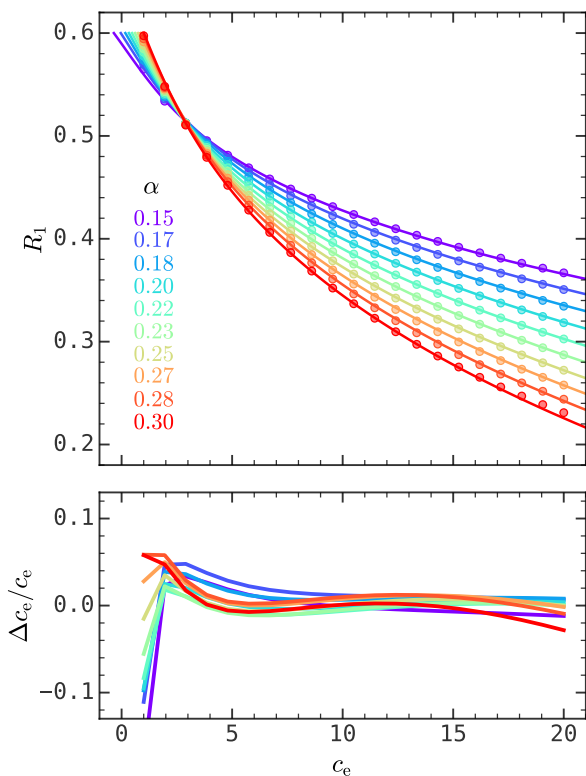


**Figure 9.** The relation between  $R_1$  and the concentration parameter of the Einasto profile,  $c_e$ , for different values of  $\alpha$  (see equation (12)). The solid lines are the fitting function in equation (15).

of  $\approx 0.28$  dex between unrelaxed halos of lower concentration and relaxed ones with higher concentration. The standard deviations of the logarithmic concentration for relaxed and unrelaxed halos are  $\approx 0.12$  dex and  $\approx 0.19$  dex, respectively, with a weak dependence on halo mass. (see Figs. 5, 6, and 7).

(v) The maximum circular velocity,  $V_{\max}$ , of simulated halos can be derived from  $R_1$  efficiently. The  $V_{\max} - R_1$  relation is not affected by whether or not the halo in question is about to be accreted by another halo and to become a subhalo (see Fig. 8 and Appendix H).

(vi) We find a fitting function for the relation between  $R_1$  and the Einasto concentration  $c_e = r_{\text{vir}}/r_{-2}$  with  $0.15 \leq \alpha \leq 0.3$ , and the fractional deviation is  $\lesssim 5\%$  for  $c \gtrsim 3$  and  $\lesssim 10\%$  for  $c \lesssim 3$  (see Fig. 9).

The concentration parameter and related structural quantities of dark matter halos play an important role in the study of dark matter halos and the modeling of the galaxy-halo connection. However, because of the uncertainty and tedium in their estimations, many cosmological simulations run in large boxes with relatively low resolutions avoid providing these quantities. The  $R_1$  method proposed here can fill the gap, as it provides an accurate proxy for the concentration parameter for both NFW and Einasto halos. Its estimation is both straightforward and efficient, thus suitable for large cosmological simulations, such as MillenniumTNG (Bose et al. 2023) and FLAMINGO (Schaye et al. 2023). We suggest that this quantity be provided in simulated halo catalogs along with other important halo properties.

## ACKNOWLEDGEMENTS

Kai Wang thanks Fangzhou Jiang for his helpful comments and suggestions. The authors acknowledge the Tsinghua Astrophysics High-Performance Computing platform at Tsinghua University for providing computational and data storage resources that have contributed to the research results reported within this paper. This work is supported by the National Science Foundation of China (NSFC) Grant No. 12125301, 12192220, 12192222, and the science research grants from the China Manned Space Project with NO. CMS-CSST-2021-A07. YC is supported by China Postdoctoral Science Foundation Grant No. 2022TQ0329 and NSFC Grant No. 12192224.

The computation in this work is supported by the HPC toolkits HIPP (Chen & Wang 2023) and PyHIPP<sup>4</sup>, IPYTHON (Perez & Granger 2007), MATPLOTLIB (Hunter 2007), NUMPY (van der Walt et al. 2011), SCIPY (Virtanen et al. 2020), ASTROPY (Astropy Collaboration et al. 2013, 2018, 2022). This research made use of NASA’s Astrophysics Data System for bibliographic information. The authors thank ELUCID collaboration for making their data products publicly available<sup>5</sup>.

## DATA AVAILABILITY

The data underlying this article will be shared on reasonable request to the corresponding author.

## REFERENCES

- Astropy Collaboration et al., 2013, *A&A*, 558, A33  
 Astropy Collaboration et al., 2018, *AJ*, 156, 123  
 Astropy Collaboration et al., 2022, *apj*, 935, 167  
 Baugh C. M., 2006, *Reports on Progress in Physics*, 69, 3101  
 Bhattacharya S., Habib S., Heitmann K., Vikhlinin A., 2013, *The Astrophysical Journal*, 766, 32  
 Binney J., Tremaine S., 2008, *Galactic Dynamics: Second Edition*  
 Bose S., et al., 2023, *Monthly Notices of the Royal Astronomical Society*, 524, 2579  
 Bullock J. S., Kolatt T. S., Sigad Y., Somerville R. S., Kravtsov A. V., Klypin A. A., Primack J. R., Dekel A., 2001, *Monthly Notices of the Royal Astronomical Society*, 321, 559  
 Chen Y., Wang K., 2023, HIPP: High-Performance Package for scientific computation, Astrophysics Source Code Library, record ascl:2301.030 (ascl:2301.030)  
 Chen Y., Mo H. J., Li C., Wang H., Yang X., Zhang Y., Wang K., 2020, *The Astrophysical Journal*, 899, 81  
 Child H. L., Habib S., Heitmann K., Frontiere N., Finkel H., Pope A., Morozov V., 2018, *The Astrophysical Journal*, 859, 55  
 Correa C. A., Wyithe J. S. B., Schaye J., Duffy A. R., 2015, *Monthly Notices of the Royal Astronomical Society*, 452, 1217  
 Davis M., Efstathiou G., Frenk C. S., White S. D. M., 1985, *The Astrophysical Journal*, 292, 371  
 Davis A. J., D’Aloisio A., Natarajan P., 2011, *Monthly Notices of the Royal Astronomical Society*, 416, 242  
 Diemer B., 2018, *ApJS*, 239, 35  
 Diemer B., Joyce M., 2019, *The Astrophysical Journal*, 871, 168  
 Duffy A. R., Schaye J., Kay S. T., Dalla Vecchia C., 2008, *Monthly Notices of the Royal Astronomical Society*, 390, L64  
 Einasto J., 1965, *Trudy Astrofizicheskogo Instituta Alma-Ata*, 5, 87  
 Fakhouri O., Ma C.-P., 2008, *Monthly Notices of the Royal Astronomical Society*, 386, 577

<sup>4</sup> <https://github.com/ChenYangyao/pyhipp>

<sup>5</sup> <https://www.elucid-project.com/>

Gao L., Navarro J. F., Cole S., Frenk C. S., White S. D. M., Springel V., Jenkins A., Neto A. F., 2008, *Monthly Notices of the Royal Astronomical Society*, 387, 536

Huchra J. P., Geller M. J., 1982, *The Astrophysical Journal*, 257, 423

Hunter J. D., 2007, *Computing in Science & Engineering*, 9, 90

Ishiyama T., et al., 2021, *Monthly Notices of the Royal Astronomical Society*, 506, 4210

Jing Y. P., 2000, *The Astrophysical Journal*, 535, 30

Jing Y. P., Suto Y., 2002, *The Astrophysical Journal*, 574, 538

Klypin A., Kravtsov A. V., Bullock J. S., Primack J. R., 2001, *The Astrophysical Journal*, 554, 903

Klypin A. A., Trujillo-Gomez S., Primack J., 2011, *The Astrophysical Journal*, 740, 102

Klypin A., Yepes G., Gottlöber S., Prada F., Heß S., 2016, *Monthly Notices of the Royal Astronomical Society*, 457, 4340

Lang M., Holley-Bockelmann K., Sinha M., 2015, *The Astrophysical Journal*, 811, 152

Lu Y., Mo H. J., Katz N., Weinberg M. D., 2006, *Monthly Notices of the Royal Astronomical Society*, 368, 1931

Ludlow A. D., Bose S., Angulo R. E., Wang L., Hellwing W. A., Navarro J. F., Cole S., Frenk C. S., 2016, *Monthly Notices of the Royal Astronomical Society*, 460, 1214

Ludlow A. D., Schaye J., Bower R., 2019, *Monthly Notices of the Royal Astronomical Society*, 488, 3663

Mansfield P., Avestruz C., 2021, *Monthly Notices of the Royal Astronomical Society*, 500, 3309

Matthee J., Schaye J., Crain R. A., Schaller M., Bower R., Theuns T., 2017, *Monthly Notices of the Royal Astronomical Society*, 465, 2381

Mo H., Van den Bosch F., White S., 2010, *Galaxy Formation and Evolution*. Cambridge University Press, Cambridge ; New York

Navarro J. F., Frenk C. S., White S. D. M., 1997, *The Astrophysical Journal*, 490, 493

Navarro J. F., et al., 2004, *Monthly Notices of the Royal Astronomical Society*, 349, 1039

Nelson D., et al., 2019, *Computational Astrophysics and Cosmology*, 6, 2

Neto A. F., et al., 2007, *Monthly Notices of the Royal Astronomical Society*, 381, 1450

Perez F., Granger B. E., 2007, *Computing in Science & Engineering*, 9, 21

Pillepich A., et al., 2018, *MNRAS*, 475, 648

Planck Collaboration et al., 2016, *Astronomy & Astrophysics*, 594, A13

Poveda-Ruiz C. N., Forero-Romero J. E., Muñoz-Cuarteras J. C., 2016, *The Astrophysical Journal*, 832, 169

Power C., Navarro J. F., Jenkins A., Frenk C. S., White S. D. M., Springel V., Stadel J., Quinn T., 2003, *Monthly Notices of the Royal Astronomical Society*, 338, 14

Prada F., Klypin A. A., Cuesta A. J., Betancort-Rijo J. E., Primack J., 2012, *Monthly Notices of the Royal Astronomical Society*, 423, 3018

Reddick R. M., Wechsler R. H., Tinker J. L., Behroozi P. S., 2013, *The Astrophysical Journal*, 771, 30

Schaye J., et al., 2023, *Monthly Notices of the Royal Astronomical Society*

Springel V., White S. D. M., Tormen G., Kauffmann G., 2001, *Monthly Notices of the Royal Astronomical Society*, 328, 726

Springel V., et al., 2005, *Nature*, 435, 629

Tweed D., Yang X., Wang H., Cui W., Zhang Y., Li S., Jing Y. P., Mo H. J., 2017, *The Astrophysical Journal*, 841, 55

Virtanen P., et al., 2020, *Nature Methods*, 17, 261

Wang H., Mo H. J., Yang X., van den Bosch F. C., 2013, *The Astrophysical Journal*, 772, 63

Wang H., Mo H. J., Yang X., Jing Y. P., Lin W. P., 2014, *The Astrophysical Journal*, 794, 94

Wang H., et al., 2016, *The Astrophysical Journal*, 831, 164

Wang K., Mao Y.-Y., Zentner A. R., Lange J. U., van den Bosch F. C., Wechsler R. H., 2020a, *Monthly Notices of the Royal Astronomical Society*, 498, 4450

Wang J., Bose S., Frenk C. S., Gao L., Jenkins A., Springel V., White S. D. M., 2020b, *Nature*, 585, 39

Wechsler R. H., Tinker J. L., 2018, *Annual Review of Astronomy and Astrophysics*, 56, 435

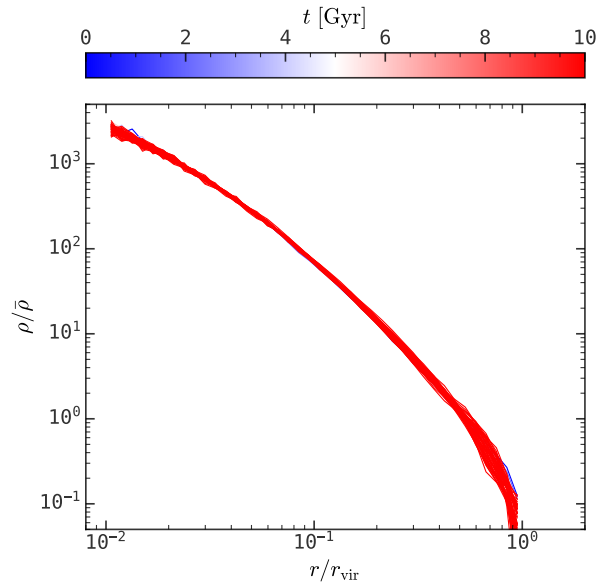


**Figure A1.** The time evolution of the density profile of a halo with 10,000 particles generated from the HALOFACTORY package from 0 to 10 Gyr.

Wechsler R. H., Bullock J. S., Primack J. R., Kravtsov A. V., Dekel A., 2002, *The Astrophysical Journal*, 568, 52

York D. G., et al., 2000, *The Astronomical Journal*, 120, 1579

Zehavi I., Kerby S. E., Contreras S., Jiménez E., Padilla N., Baugh C. M., 2019, *The Astrophysical Journal*, 887, 17

Zhao D. H., Mo H. J., Jing Y. P., Börner G., 2003a, *Monthly Notices of the Royal Astronomical Society*, 339, 12

Zhao D. H., Jing Y. P., Mo H. J., Börner G., 2003b, *The Astrophysical Journal*, 597, L9

Zhao D. H., Jing Y. P., Mo H. J., Börner G., 2009, *The Astrophysical Journal*, 707, 354

van den Bosch F. C., Jiang F., 2016, *Monthly Notices of the Royal Astronomical Society*, 458, 2870

van den Bosch F. C., Ogiya G., Hahn O., Burkert A., 2018, *Monthly Notices of the Royal Astronomical Society*, 474, 3043

van der Walt S., Colbert S. C., Varoquaux G., 2011, *Computing in Science & Engineering*, 13, 22

## APPENDIX A: GENERATE DARK MATTER HALOS WITH HALOFACTORY

Here we present an open-source Python package, HALOFACTORY<sup>6</sup>, which implements the algorithms for generating the position and velocity of particles in mock halos. These halos are assumed to be collisionless and spherically symmetric systems in dynamical equilibrium, whose behavior can be described by the collisionless Boltzmann equation (Binney & Tremaine 2008). HALOFACTORY uses Eddington’s inversion method to sample the position and velocity of particles from the exact phase-space distribution function, which is more accurate than approximation methods that rely on the Jeans equations (Binney & Tremaine 2008). In addition, HALOFACTORY is rather efficient due to the adoption of various numerical acceleration techniques. Finally, HALOFACTORY can serve various

<sup>6</sup> <https://github.com/ChenYangyao/halofactory>

purposes, such as providing initial conditions for numerical simulations and serving as input for halo-based galaxy models. Fig. A1 shows the time evolution of the density profile of a halo generated from HALOFAC<sub>TORY</sub> with 10,000 particles and an initial concentration of 15. Here one can see that the density profile has nearly no evolution on a time scale of 10 Gyr, which indicates that the halos generated from HALOFAC<sub>TORY</sub> are already in equilibrium.

The implementation of HALOFAC<sub>TORY</sub> relies on Eddington's formula. For an equilibrium and spherical system given by the density distribution  $\rho(r)$ , the particle energy distribution is given by

$$f(E) = \frac{1}{\sqrt{8}\pi^2} \frac{d}{dE} \int_E^{E_T} dV \frac{1}{V-E} \frac{d\rho(V)}{dV}, \quad (\text{A1})$$

which is called Eddington's formula (see chapter 4 in Binney & Tremaine 2008). Here  $E$  is the particle energy and  $V$  is the potential energy. We also require the maximum energy of particles  $E_T$  equals to the potential energy at the truncation radius  $r_T$ , which is a free parameter, so that particles are restrained within  $r_T$ . In HALOFAC<sub>TORY</sub>, the sampling of particle position and velocity are proceeded as follows:

- **Sampling particle position:** We can integrate the radial density profile  $\rho(r)$  to get the accumulative mass distribution, which is  $M(< r) = \int_0^r 4\pi x^2 \rho(x) dx$ . Then we generate random numbers  $\mathcal{R}_0$ , which are uniformly distributed between 0 and 1, and solve  $\mathcal{R}_0 = M(< r)/M(< r_T)$  to get the radial distance. Finally, we randomly sample orientations  $(\theta, \phi)$ , which are uniformly distributed on a sphere, and the tuples of  $(r, \theta, \phi)$  can specify the positions of particles.

- **Sampling particle velocity:** The sampling of particle velocities relies on Eddington's formula, which is numerically calculated and tabulated at first<sup>7</sup>. We first generate three random numbers  $\mathcal{R}_1$ ,  $\mathcal{R}_2$  and  $\mathcal{R}_3$ , which are uniformly distributed between 0 and 1. Then we can get the radial velocity  $v_r$  and tangential velocity  $v_t$  through solving

$$\mathcal{R}_1 = \frac{3}{4} \left[ \frac{v_r}{v_{\max}} - \frac{1}{3} \left( \frac{v_r}{v_{\max}} \right)^3 \right] + \frac{1}{2} \quad (\text{A2})$$

$$\mathcal{R}_2 = \frac{v_t^2}{v_{\max}^2 - v_r^2} \quad (\text{A3})$$

where  $v_{\max}(r) = \sqrt{2(E_T - V(r))}$  is the maximum velocity. Then we evaluate

$$\frac{f\left(v_r^2/2 + v_t^2/2 + V(r)\right)}{f(V(r))} > \mathcal{R}_3, \quad (\text{A4})$$

then we accept the velocity tuple  $(v_r, v_t)$  if the above assertion is true and otherwise discard it. Finally, we generate an orientation on the plane perpendicular to  $\hat{\mathbf{r}}$  for the tangential velocity component.

## APPENDIX B: IMPACT OF BINNING ON NFW PROFILE FITTING

Fig. B1 shows the fractional concentration deviation for the NFW profile fitting method on ideal NFW halos generated from HALOFAC<sub>TORY</sub>, and the three rows correspond to the following binning strategies

(i)  $(0.01 - 1r_{\text{vir}}, \log)$ : 20 equally spaced radial bins on a logarithmic scale from  $0.01r_{\text{vir}}$  to  $r_{\text{vir}}$ , which is used in the main body of the paper);

(ii)  $(0.1 - 1r_{\text{vir}}, \log)$ : 20 equally spaced radial bins on a logarithmic scale from  $0.1r_{\text{vir}}$  to  $r_{\text{vir}}$  (e.g. Bhattacharya et al. 2013);

(iii)  $(0 - 1r_{\text{vir}}, \text{linear})$ : 20 equally spaced radial bins on a linear scale from 0 to  $r_{\text{vir}}$  (e.g. Chen et al. 2020);

As one can see, the bias in the first and last binning methods converges to zero as the particle number increases, but the second binning method underestimates the halo concentration, especially for high-concentration halos. This happens because the second method does not fit the inner density distribution. As the particle number decreases to a few hundred, all three methods produce systematics at the level of  $\approx 10 - 20\%$ , and the sign of the systematics depends both on the binning method and the concentration of the input halo. These results demonstrate that it is not straightforward to find an optimal binning to achieve a reliable estimation of the halo concentration, particularly when individual halos are only sampled by a small number of particles.

## APPENDIX C: OTHER METHODS TO ESTIMATE HALO CONCENTRATION

**Maximum likelihood:** We propose to use the maximum likelihood method to estimate the concentration parameter of NFW halos. To begin with, the NFW differential mass profile is given by

$$\frac{dM(< r)}{dr} = \frac{M_{\text{vir}}}{r_{\text{vir}}} \frac{x}{m(c)(c^{-1} + x)^2}. \quad (\text{C1})$$

where  $m(c) = \ln(1+c) - c/(1+c)$ ,  $x = r/r_{\text{vir}}$ . Then, for a set of particles, each represented by the normalized radial location  $x_i = r_i/r_{\text{vir}}$ , one can express the logarithmic likelihood function as

$$\ln \mathcal{L} \propto \sum_i \left[ \ln(x_i) - \ln m(c) - 2 \ln(c^{-1} + x_i) \right]. \quad (\text{C2})$$

The concentration parameter can then be estimated by maximizing this likelihood function. We note that the maximum likelihood method is unambiguous and applicable to different halo profiles. However, the summation in the likelihood function needs to be evaluated in each iteration of the optimization, which makes this method computationally expensive, especially for finely sampled halos.

**Peak finding:** The NFW differential mass profile (see equation (C1)) peaks at  $r = r_s$ , so the concentration parameter  $c = r_{\text{vir}}/r_s$  can be inferred by locating the peak of equation (C1) (e.g. Child et al. 2018). In order to suppress the noise for poorly sampled halos, we first smooth the differential mass profile with a three-point Hanning filter, which is

$$f(r_i) = \frac{1}{4} [f(r_{i-1}) + 2f(r_i) + f(r_{i+1})]. \quad (\text{C3})$$

Here we calculate the NFW differential mass profile with 20 bins from  $0.01r_{\text{vir}}$  to  $r_{\text{vir}}$  on a logarithmic scale, and the two bins at both ends are dropped after the smoothing step. In this case, the peak is constrained within  $0.014r_{\text{vir}}$  and  $0.713r_{\text{vir}}$ , so that the minimum and maximum concentrations that can be recovered are 1.4 and 70.3. We note that the result obtained here is subject to the choice of binning.

<sup>7</sup> We refer to Prof. Martin Weinberg's lecture note for the detailed derivation in <https://courses.umass.edu/astron850-mdw/eddington.pdf>.

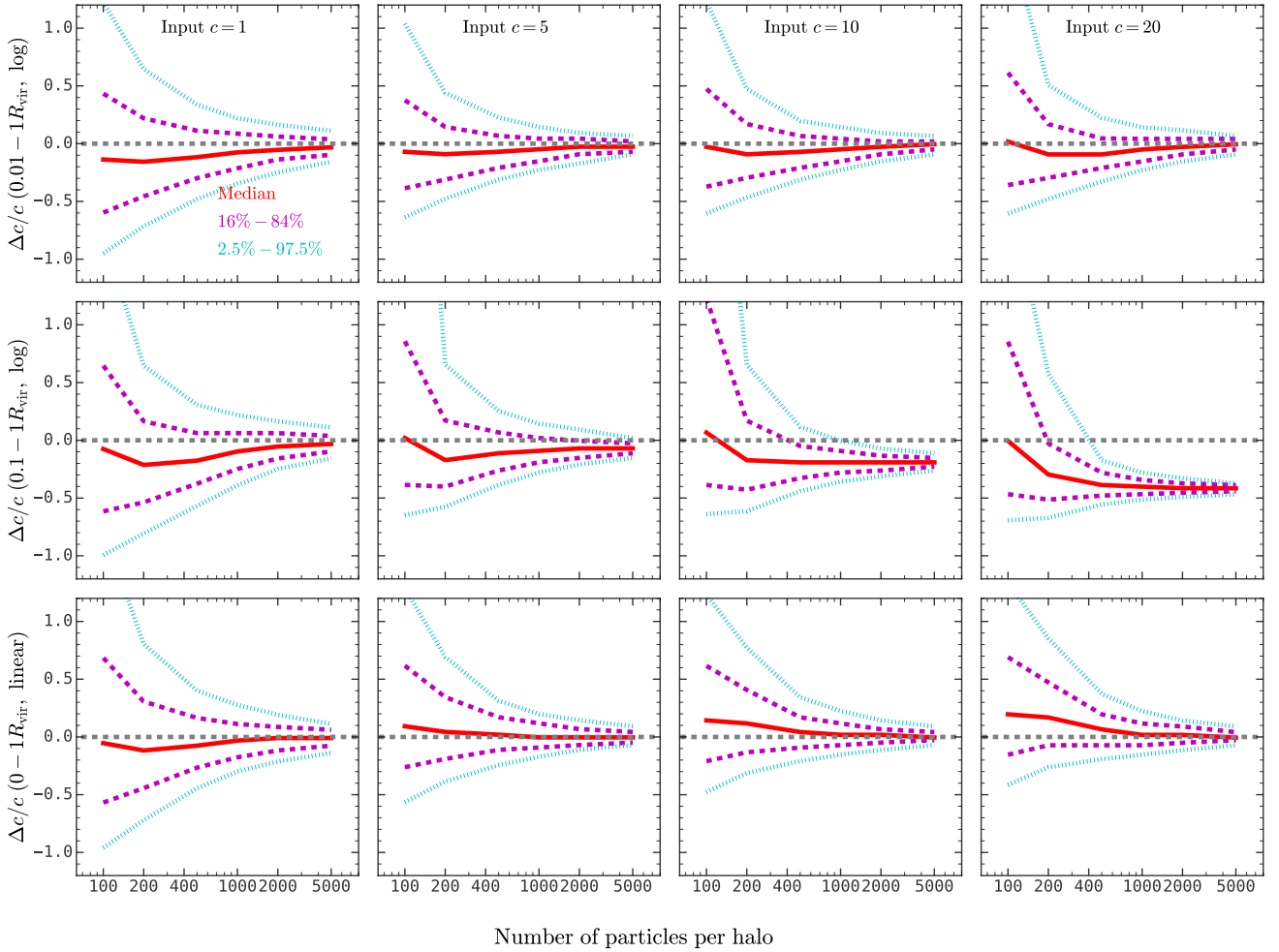


**Figure B1.** Similar to Fig. 2, except that different rows are the results obtained from the NFW profile fitting method with different binning strategies: binning on a logarithmic scale within  $0.01 - 1r_{\text{vir}}$  (top panels), binning on a logarithmic scale within  $0.1 - 1r_{\text{vir}}$  (middle panels), and binning on a linear scale within  $0 - 1r_{\text{vir}}$  (bottom panels).

**Cumulative mass:** For ideal NFW halos, the half-mass radius  $r_h$ , which encloses half of the total halo mass, is given by

$$\frac{1}{2} = \frac{g(r_h)}{g(r_{\text{vir}})}, \quad (\text{C4})$$

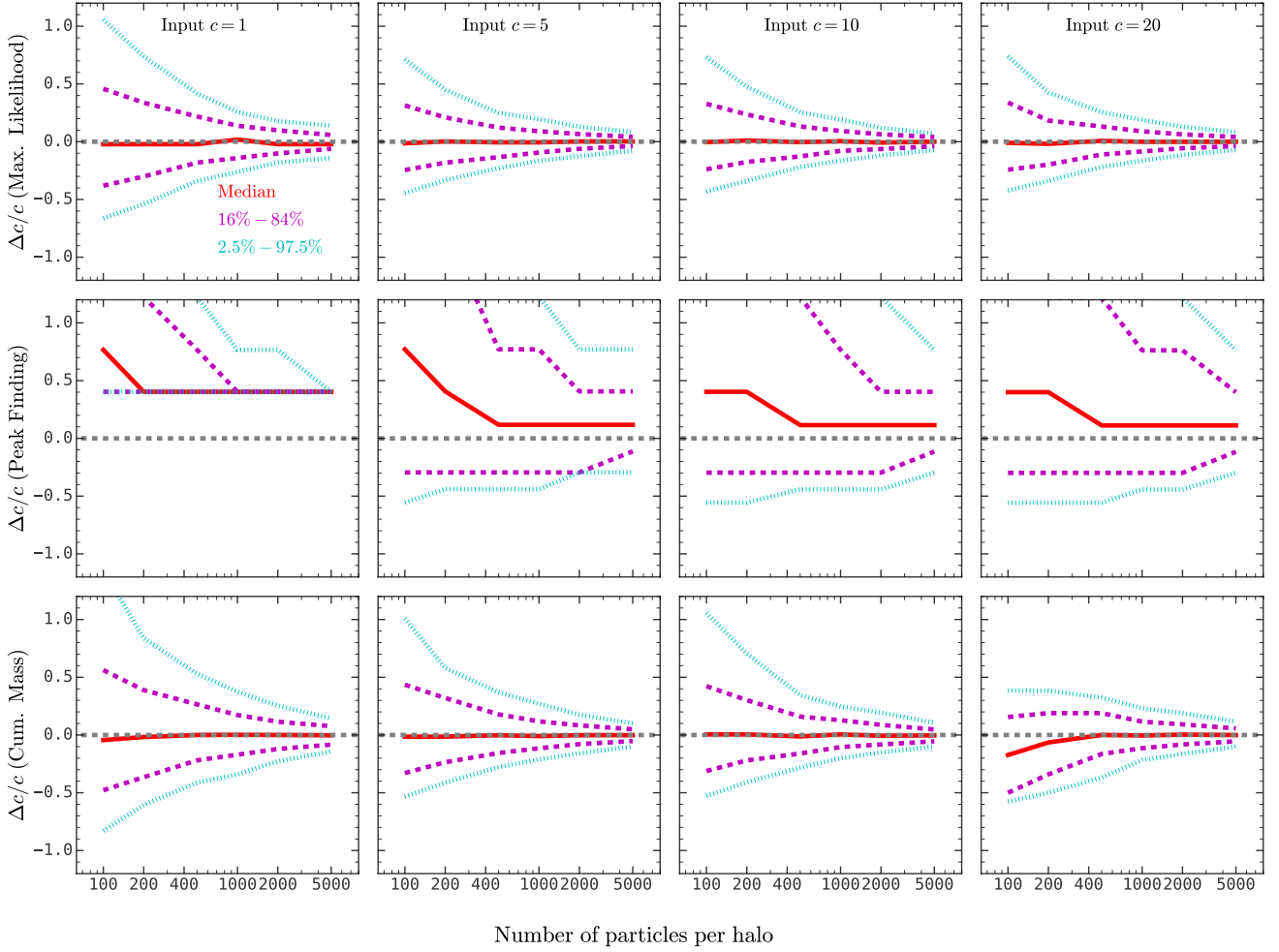
where  $g(x) = \ln[(r_s + x)/r_s] - x/(r_s + x)$ . Therefore, the concentration parameter can be inferred through  $r_s$  by numerically solving this equation (e.g. Lang et al. 2015).

Fig. C1 shows the performance of these three methods of concentration estimation on ideal NFW halos. Firstly, the maximum likelihood method performs the best, even outperforming our  $R_1$  method (see Fig. 2). This method can be easily generalized to other profiles. However, the optimization of the likelihood is computationally expensive, especially for finely sampled halos, since the summation of the logarithmic likelihood of all particles needs to be evaluated during each optimization iteration. Secondly, the peak finding method makes no assumption about the specific form of the halo profile. However, this method performs poorly with large systematics and scatter, since it requires the evaluation of the (differential) density profile, which poses challenges to the choice of binning: a large bin size will not sample both ends well, while a small bin size will cause large shot noise. Finally, the cumulative

method performs quite well, except for the  $\approx 20\%$  systematics for poorly sampled high-concentration halos. Moreover, this method requires numerically solving a non-linear equation, whose complexity is comparable to the conventional NFW profile fitting method.

#### APPENDIX D: UNCERTAINTIES OF THE $R_1$ METHOD

Here we quantify the statistical uncertainties of our  $R_1$  method in estimating halo concentration for ideal NFW halos. Fig. D1 shows the distribution of the logarithmic deviation of the estimated concentration with our  $R_1$  method from the true concentration of ideal NFW halos. For each input concentration and particle number, we generate 10,000 realizations of NFW halos and estimate their concentration based on equations 3 and 4. The logarithmic deviation is shown in the gray histogram. We then calculate the standard



**Figure C1.** Similar to Fig. 2, except for three other methods to estimate halo concentration: the maximum likelihood method (top panels), the peak finding method (middle panels), and the cumulative mass method (bottom panels).

deviation of the logarithmic deviation as follows:

$$\sigma = \sqrt{\frac{1}{N_{\text{samp}}} \sum_{i=1}^{N_{\text{samp}}} \Delta_i^2} \quad (\text{D1})$$

$$\Delta_i = \log(c_{\text{est},i} + 1) - \log(c_{\text{input}} + 1)$$

where  $N_{\text{samp}} = 10,000$  in this case. Finally, we over-plot the probability distribution function of a Gaussian distribution with a mean of 0 and a standard deviation of  $\sigma$  in each panel. Here one can see that this Gaussian distribution matches the histogram very well.

Fig. D2 shows the relation between  $\sigma$  and the sampling particle number for four different input concentrations. Here one can see that  $\sigma$  is about 0.10–0.15 dex for halos sampled with only 100 particles. With increasing sampling, the uncertainty of the concentration estimation rapidly decreases, to a value of 0.01 dex when the number of particles reaches  $2 \times 10^4$ . We also find that the dependence of  $\sigma$  on the particle number and the input concentration can be fitted

with

$$\sigma(c, N_{\text{part}}) = \frac{a_1(c)}{(\log N_{\text{part}})^2} + \frac{a_2(c)}{\log N_{\text{part}}} \quad (\text{D2})$$

$$a_1(c) = 0.330c + 0.515$$

$$a_2(c) = -0.063c - 0.095$$

where  $N_{\text{part}}$  is the particle number. And this function is over-plotted in Fig. D2 as solid lines.

## APPENDIX E: DENSITY PROFILE FOR LOW-MASS AND HIGH-CONCENTRATION HALOS

In order to understand the discrepancy in the concentration estimated from the NFW fitting method and our  $R_1$  method for low-mass high-concentration halos in Fig. 4, we select high-concentration halos with  $11 \leq \log(M_{200c}/[h^{-1}M_{\odot}]) < 11.5$  from TNG50-1-Dark and plot their density distribution in the right panels of Fig. E1. For comparison, we also plot the density distribution of low-concentration halos in the same mass range (left panels). Here one can see that the mass distribution of high-concentration halos deviates from the NFW profile due to stripping in the outskirts of

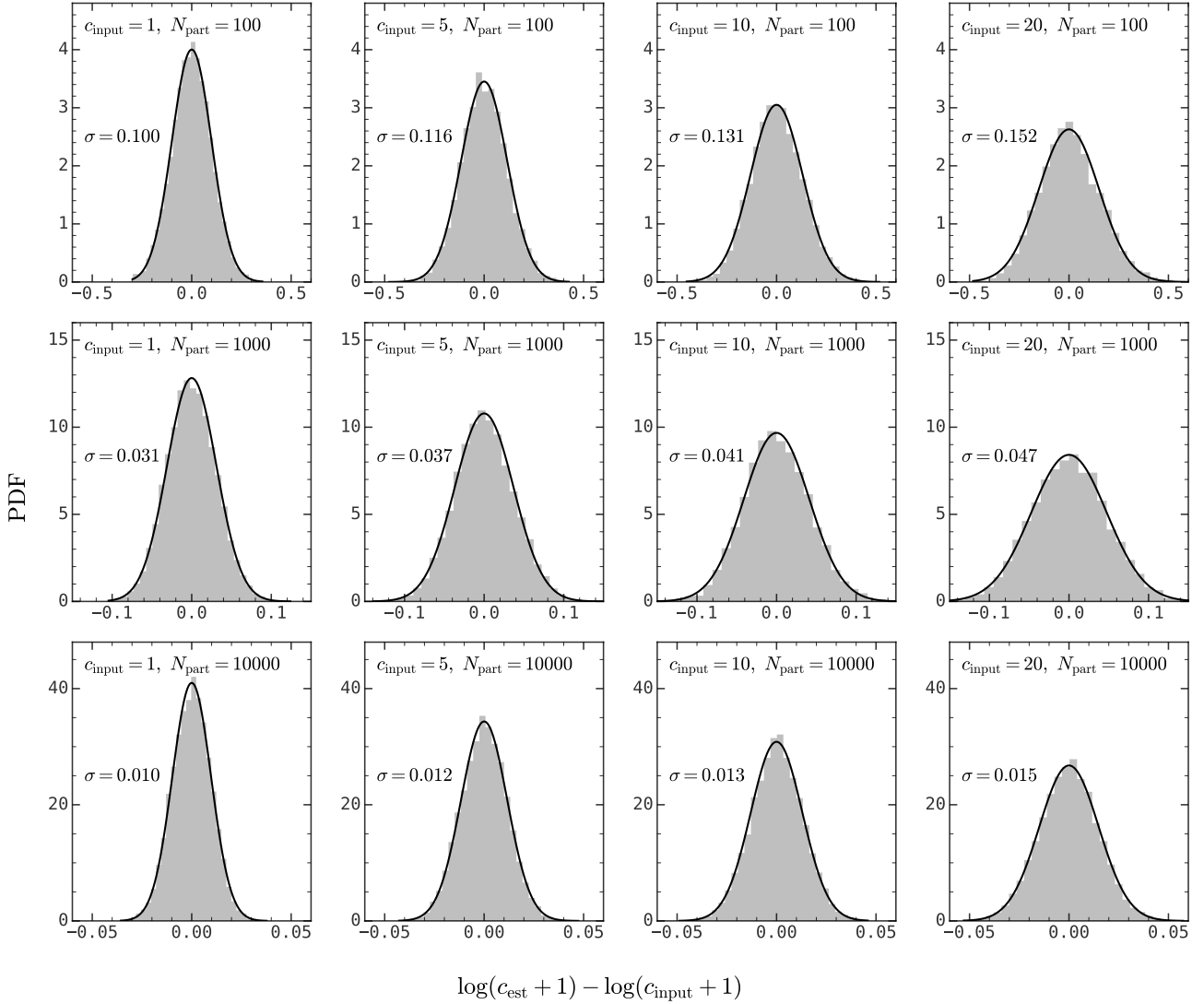


**Figure D1.** Probability distributions of the deviation of the concentration estimated using the  $R_1$  method,  $c_{\text{est}}$  from the input concentration,  $c_{\text{input}}$  for different  $c_{\text{input}}$  (different columns) and different numbers of particles (different rows); note the different  $x$ -axis ranges. In each panel, the distribution of  $\log(c_{\text{est}} + 1) - \log(c_{\text{input}} + 1)$  is shown as a gray histogram, and the standard deviation,  $\sigma$ , calculated with equation (D1) is indicated. A Gaussian distribution of  $\mathcal{N}(\mu = 0, \sigma = \sigma)$  is shown in black solid line. This figure shows that the logarithmic deviation of the estimated concentration from the true concentration can be described by a Gaussian distribution.

halos. The density and mass distributions reconstructed from both NFW fitting and  $R_1$  methods match the data equally well, despite the  $(18.74 - 16.32)/18.74 \approx 13\%$  systematics between their results.

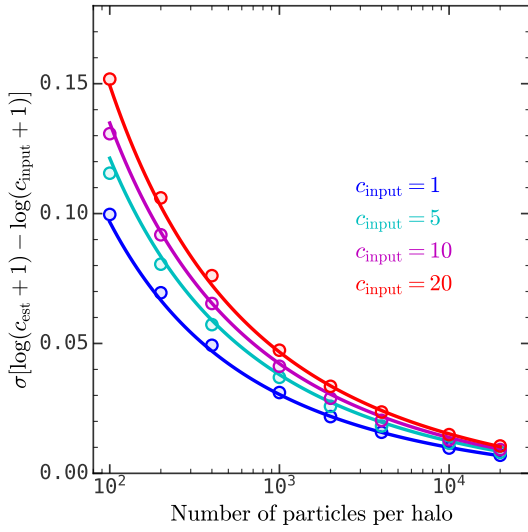
#### APPENDIX F: IMPACT OF COSMOLOGY ON THE MASS-CONCENTRATION RELATION

Fig. F1 shows the mass-concentration relation for different cosmological parameters generated from the analytical model in Zhao et al. (2009). Here one can see that the cosmology adopted by TNG yields higher concentrations than that of ELUCID at a given halo mass, as we see in Figs. 3 and 5. The bottom panel shows the ratio between these two analytical relations as the black solid line, and the error bars show the ratio between the mass-concentration relations for simulated halos in TNG100-1-Dark and ELUCID. The two ratios

are broadly consistent with each other, indicating that the difference in the mass-concentration relation between TNG100-1-Dark and ELUCID is caused by the different cosmological parameters they adopt.

#### APPENDIX G: ESTIMATING $c_{200c}$ FROM $c_{500c}$

Fig. G1 shows the relation between the concentrations obtained from equations 3 and 4 with  $r_{\text{vir}} = r_{200c}$  and  $r_{\text{vir}} = r_{500c}$ , which are the radius within which the mean density is 200 and 500 times the critical density, respectively. And the corresponding halo masses are  $M_{200c}$  and  $M_{500c}$ . The relation between  $c_{200c}$  and  $c_{500c}$  is fitted



**Figure D2.** The standard deviation of  $\log(c_{\text{est}} + 1) - \log(c_{\text{input}} + 1)$  as a function of particle number per halo for different input concentrations, where  $c_{\text{est}}$  is estimated with our  $R_1$  method. The circles are results obtained with equation (D1) for ideal NFW halos. The solid lines are the fitting results of equation (D2).

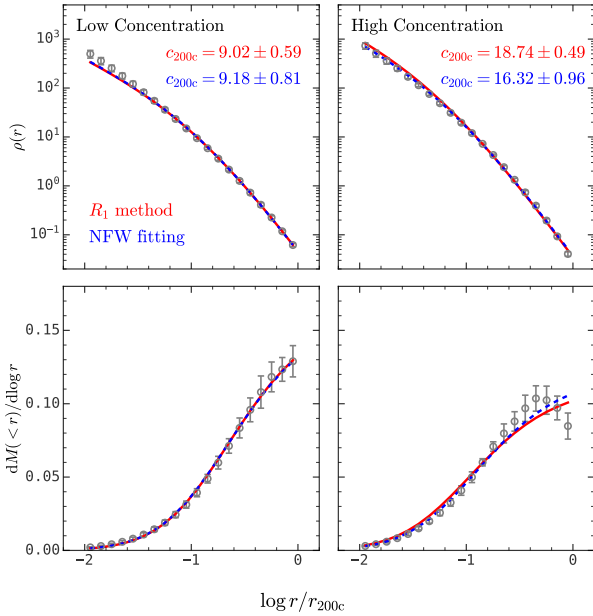


**Figure E1.** The density distribution of low-concentration (left panels) and high-concentration (right panels) halos with  $11 \leq \log(M_{200c}/[h^{-1}M_{\odot}]) < 11.5$  selected from TNG50-1-Dark. The top panels and bottom panels show the density distributions and the mass distributions, respectively. The red solid and blue dashed lines show the NFW profile from the mean concentration of each subsample, where the concentration is estimated with our  $R_1$  method and the NFW fitting method, respectively. This figure demonstrates that the discrepancy of concentration estimation from the NFW fitting method and our  $R_1$  method for low-mass and high-concentration halos in Fig. 4 is attributed to the deviation from the NFW distribution due to the stripping of the halo outer regions.

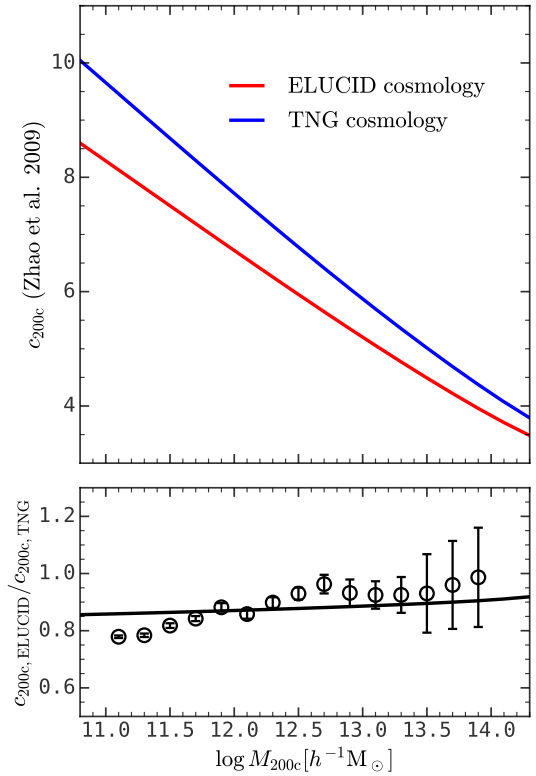


**Figure F1.** Top panel: The mass-concentration relation generated from the analytical model in Zhao et al. (2009) with the cosmological parameter values used in TNG100-1-Dark and ELUCID (see § 2). Bottom panel: The ratio between the mass-concentration relations from two different sets of cosmological parameters. The black solid line is the prediction of the model from Zhao et al. (2009), and the black error bars are the result obtained from simulations. The difference of the mass-concentration relation in TNG100-1-Dark and ELUCID can be attributed to the difference in their cosmological parameters.

with

$$c_{200c} = g_1 c_{500c}^2 + g_2 c_{500c} + g_3, \quad (\text{G1})$$

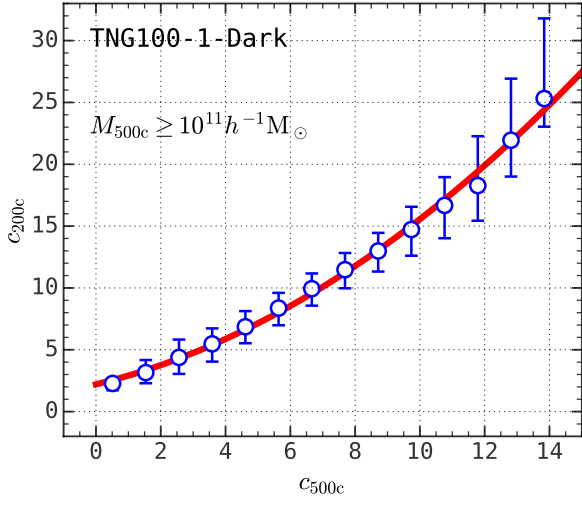
$$g_1 = 0.070, \quad g_2 = 0.638, \quad g_3 = 2.202,$$

which has marginal dependence on halo mass. With this relation, we can infer the concentration parameter  $c_{200c}$  by integrating equation (3) only to  $r_{500c}$ .

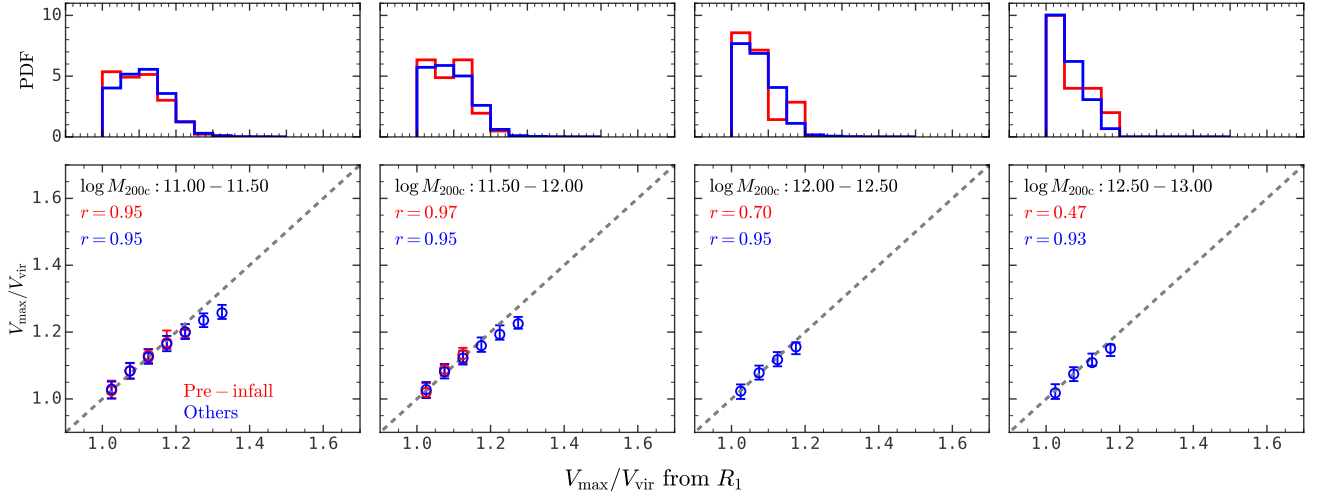
## APPENDIX H: $V_{\text{MAX}}$ ESTIMATION FOR PRE-INFALL HALOS

Fig. H1 compares  $V_{\text{max}}/V_{\text{vir}}$  calculated from equation (9) and estimated from  $R_1$  for halos selected from TNG100-1-Dark at  $z = 0.7$ . Here halos are divided into two subsamples: “pre-infall” halos are those that will be accreted onto other halos to become subhalos in the next snapshot; “others” are halos excluding “pre-infall” halos. No additional systematics are seen for pre-infall halos, indicating that environmental effects on super-halo scales have insignificant effects on the estimation of  $V_{\text{max}}/V_{\text{vir}}$  from  $R_1$ .

This paper has been typeset from a  $\text{\TeX}/\text{\LaTeX}$  file prepared by the author.



**Figure G1.** The relation between the concentrations obtained from equations 3 and 4 with  $r_{\text{vir}} = r_{200c}$  and  $r_{\text{vir}} = r_{500c}$ . The blue error bars show the 16<sup>th</sup> – 50<sup>th</sup> – 86<sup>th</sup> percentiles and the red solid line is the fitting function in equation (G1).



**Figure H1.** Similar to Fig. 8, except that these halos are selected from TNG100-1-Dark at  $z = 0.7$ . Red error bars are for halos that will be accreted by other halos and become a satellite subhalo at the next snapshot, and blue error bars are for the remaining halos. The environmental effects before accretion do not affect the estimation of  $V_{\max}/V_{\text{vir}}$  from  $R_1$ .